Ozone and water vapor variability in the polar middle atmosphere observed with ground-based microwave radiometers

Guochun Shi[1], Witali Krochin[1], Eric Sauvageat[1], and Gunter Stober[1]

[1]Institute of Applied Physics & Oeschger Center for Climate Change Research, University of Bern, Bern, Switzerland

Correspondence: Guochun Shi (guochun.shi@unibe.ch)

Abstract. We present continuous ozone and water vapor measurements with the two ground-based radiometers GROMOS-C and MIAWARA-C at Ny-Ålesund, Svalbard (79°N, 12°E), that started in September 2015. Leveraging GROMOS-C and MIAWARA-C measurements, MERRA-2, and Aura-MLS datasets, we analyze the long-term behavior and interannual differences of ozone and water vapor and compile climatologies of both trace gases that describe the annual variation of ozone and water vapor at polar latitudes. A climatological comparison of the measurements from our ground-based radiometers with reanalysis and satellite data was performed. Overall differences between GROMOS-C and Aura-MLS ozone climatology are on the order of 10-15 % depending on the altitudes. For the water vapor climatology, MIAWARA-C shows the best agreement with Aura-MLS on average within 5 % throughout the upper stratosphere and mesosphere. The comparison to MERRA-2 yields an agreement that reveals discrepancies larger than 50 % above 0.2 hPa depending on the implemented radiative transfer schemes and other model physics. Furthermore, we perform a conjugate latitude comparison by defining a virtual station in the southern hemisphere at the geographic coordinate (79°S, 12°E) to investigate interhemispheric differences in the atmospheric compositions. Both trace gases show much more pronounced interannual and seasonal variability in the northern hemisphere than in the southern hemisphere. We estimate the effective water vapor transport vertical velocities corresponding to upwelling and downwelling periods driven by the residual circulation. In the northern hemisphere, the water vapor ascent rate is 3.42 ± 1.89 mm s^{-1} from MIAWARA-C and 4.64 ± 1.83 mm s^{-1} from Aura-MLS, and descent rate is 4.98 ± 1.08 mm s^{-1} from MIAWARA-C and 5.40 ± 1.54 mm s^{-1} from Aura-MLS. The water vapor ascent and descent rates in the southern hemisphere are 5.22 ± 0.76 mm s^{-1} and 2.61 ± 1.44 mm s^{-1} from Aura-MLS, respectively. The water vapor transport vertical velocities analysis further reveals a higher variability in the northern hemisphere and is suitable to monitor and characterize the evolution of the northern and southern polar dynamics linked to the polar vortex as a function of time and altitude.

1 Introduction

Ozone and water vapor are essential climate variables that play a key role in the radiative balance in the middle atmosphere. Their seasonal and interannual variability is closely coupled to dynamical and chemical processes, which are driven and modulated by atmospheric waves including planetary waves, gravity waves, and atmospheric tides. These atmospheric waves transport energy and momentum from their source region to the altitudes of their dissipation and, thus, contribute to the energy balance between different atmospheric layers.

Model results suggest that gravity waves drive the summer mesopause temperature up to 100 K away from the radiative equilibrium (Lindzen, 1981; Smith, 2012; Becker, 2012). The extreme cold temperatures at the summer mesopause are the result of an upwelling, and a corresponding adiabatic cooling of the uplifted air masses, in the summer hemisphere and are accompanied by a downwelling in the winter hemisphere. The pole-to-pole circulation is often referred to as residual circulation or transformed Eulerian mean circulation (Andrews and Mcintyre, 1976). Another important circulation branch underneath the residual circulation is the Brewer-Dobson Circulation (Brewer, 1949; Dobson, 1956). The Brewer-Dobson Circulation as the major transport pattern in the stratosphere explains the variability of ozone and water vapor. The circulation is fundamentally driven by dissipating waves of tropospheric origin and broadly consists of large-scale tropical ascent and winter pole descent. The Brewer-Dobson Circulation is much weaker during boreal summer due to the different distribution of land masses and the associated differences in the generation of planetary and gravity waves between both hemispheres. The Brewer-Dobson Circulation can govern the entry and distribution of air masses and constituents from the troposphere into and within the stratosphere. The meridional transport of trace gases into the polar cap is controlled by the strength of the polar vortex, which is driven by the temperature gradient between the polar cap and the mid-latitudes through the thermal wind balance at stratospheric altitudes in the hemispheric winter, forms an essential barrier separating ozone rich air at the mid-latitudes from ozone depleted air within the polar cap. However, planetary waves can disturb the polar vortex and even lead to its breakdown during sudden stratospheric warming events (Matsuno, 1971; Baldwin et al., 2021), which is accompanied by a large-scale intrusion and mixing of air masses from the mid-latitudes towards the high-latitudes helping to recover the ozone volume mixing ratio (Schranz et al., 2020). Furthermore, the transition from the winter to the summer circulation is decisively controlled by the presence of the planetary wave activities (Matthias et al., 2021). Previous studies even concluded that dynamical forced transitions have a persistent impact on the circulation lasting several weeks (Baldwin and Dunkerton, 2001).

Stratospheric ozone observation results largely reflect the distribution that presents significant asymmetry in both hemispheres, with the differences maximizing in the winter and spring seasons (McConnell and Jin, 2008). Transport processes resulting from differences in the stratospheric ozone explain the asymmetry, as well as the interannual variability of ozone in both hemispheres (Langematz, 2019). Long-term polar ozone observations offer a better recognition and predictability of stratospheric ozone trends and an understanding of the attribution of changes. Water vapor has a chemical lifetime of the order of months in the upper stratosphere and lower mesosphere (Brasseur and Solomon, 2005), therefore, it can be used as a tracer to study the air masses dynamic. The mesosphere at the high latitudes is characterized by an annual variation with higher water vapor during local summer and lower water vapor during local winter mainly determined by the mean vertical transport (Forkman et al., 2005; Lee et al., 2011). Straub et al. (2010) and Schranz et al. (2019) estimate the vertical gradient of water vapor inside of the polar vortex in autumn based on microwave radiometry measurements at polar latitudes. Its distribution and variability exhibit a wealth of information on atmospheric circulation.

There are several techniques to obtain ozone and water vapor measurements in the middle atmosphere. The Aura satellite with the Microwave Limb Sounder (MLS) collects global water vapor and ozone profiles among other chemical species with coverage at a fixed local time due to its sun-synchronous orbit (Livesey et al., 2006). Ground-based observations are often performed using Brewer and Dobson instruments (Zuber et al., 2021), which provide very high quality and precision ozone

column densities, but lack the vertical information. Lidars are providing good vertical resolution to measure ozone (Brinksma et al., 1997; Bernet et al., 2021). The instruments carried with aircraft and balloon-borne instruments including ozonesondes and frost-point hygrometers perform highly vertically resolved measurements of ozone and water vapor in the upper tropo-sphere and lower stratosphere (Zahn et al., 2014; Eckstein et al., 2017). However, there are only a few systems available and

65 the observation time depends on tropospheric weather conditions. At tropospheric altitudes, water vapor can also be retrieved leveraging Raman-lidars (Sica and Haefele, 2015, 2016). Precise water vapor measurements above the troposphere can also be collected by in-situ balloon-borne sensors such as Laser Absorption Spectrometers (Graf et al., 2021). The ground-based microwave radiometer allows a continuous observation under all weather conditions with a high time resolution of the order of hours except during rain. It can be specially designed for measuring ozone and water vapor and operated from different

70 locations on a campaign basis (Scheiben et al., 2013, 2014) and provides datasets. Microwave radiometers can continuously measure the middle atmospheric ozone and water vapor which is valuable as it complements satellite measurements are rela-tively easy to maintain, and has a long lifetime. Ground-based microwave radiometry is the ideal technique to monitor ozone and water vapor in the Arctic/Antarctic middle atmosphere.

Here, we present a detailed comparison of ozone and water vapor measurements at conjugate latitude station leveraging mul-

75 tiyear ground-based observations from GROMOS-C and MIAWARA-C performed at Ny-Ålesund and Aura-MLS data as well as reanalysis data. We produce and compare the multiyear-mean ozone and water vapor climatologies at conjugate latitude sta-tions (Fig. 1) in the polar regions. On one hand, it is intended to provide a well-characterized representation of ozone and water vapor measured by the two instruments and the chemistry differences between both hemispheres concerning climatological behaviors. On the other hand, it provides a source of data for future work including intercomparison studies and evaluation.

80 Furthermore, we use the water vapor mixing ratios measurements from MIAWARA-C and Aura-MLS observation data to de-rive the ascent and descent rates. We estimate the strength of upwelling and downwelling in both hemispheres over the polar stations and discuss their interannual variability as well as the hemispheric differences.

We provide an overview of the datasets in section 2. The time series of ozone and water vapor at conjugate latitude stations in the Northern Hemisphere (NH) and Southern Hemisphere (SH) are presented in section 3. The climatologies of ozone and

85 water vapor are discussed in section 4. The transport of water vapor is discussed in section 5. Sections 6 and 7 present the discussion and conclusions of this study.
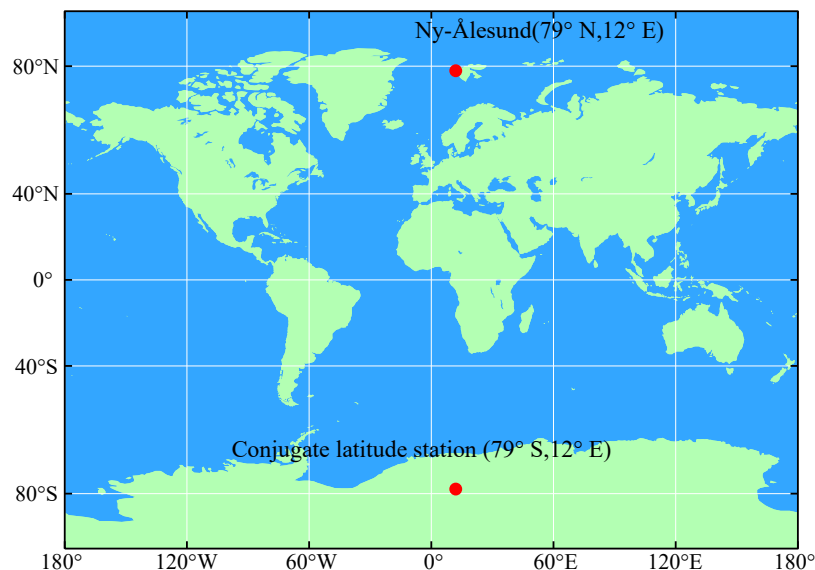
Figure 1. The geographical map indicates the two stations in the northern and southern polar regions. The conjugate latitude station in SH is a virtual station for this study. The locations of the stations are indicated with a solid red circle.

2 Instruments and models

2.1 GROMOS-C

GROMOS-C (GRound-based Ozone MOnitoring System for Campaigns) is an ozone microwave radiometer measuring the ozone emission line at 110.836 GHz at Ny-Ålesund, Svalbard (79° N, 12° E) which is described in detail in Fernández et al. (2015). It was built by the Institute of Applied Physics (IAP) at the University of Bern. GROMOS-C is designed to be very compact so that it can be transported and operated at remote field sites under extreme climate conditions. It further can switch the frequency of the local oscillator and measure the 115 GHz CO emission line. The optics of GROMOS-C has two rotating mirrors such that observations in all four cardinal directions are possible. Therefore, GROMOS-C observes subsequently on the four cardinal directions (north, east, south, and west) under an elevation angle of 22° with a sampling time of 4 s. Ozone volume mixing ratio (VMR) profiles are retrieved from the ozone spectra with a temporal averaging of 2 hours leveraging ARTS2 (Eriksson et al., 2011) and QPACK software (Eriksson et al., 2005) according to the optimal estimation algorithm (Rodgers, 2000). The sensitive altitude range for this instrument extends from 23 km to 70 km. The vertical resolution of ozone profiles is 10-12 km in the stratosphere and increases up to 20 km in the mesosphere as estimated from the width of the averaging kernels.

2.2 MIAWARA-C

MIAWARA-C (MIddle Atmospheric WAter vapor RAdiometer for Campaigns) is a ground-based microwave radiometer measuring the pressure-broadened rotational emission line of water vapor at the frequency of 22 GHz. It was also built by the University of Bern and located at Ny-Ålesund, Svalbard (79° N, 12° E). The MIAWARA-C front end is an uncooled hetero-
105 dyne receiver with a system noise temperature of 150 K. The signal is split into two polarizations by an orthomode transducer directly. The two polarized signals are analyzed in a fast Fourier transform (FFT) spectrometer model Acqiris AC240. The spectrometer has a 400 MHz bandwidth and a spectral resolution of 30.5 kHz. Similar to GROMOS-C, MIAWARA-C retrieval is also performed with ARTS2 (Eriksson et al., 2011) and QPACK software (Eriksson et al., 2005) according to the optimal estimation algorithm (Rodgers, 2000). From the measured spectra we retrieve water vapor profiles that cover an altitude range
110 extending from 37 km to 75 km with a time resolution of 2-4 h and a vertical resolution of 12-19 km. A detailed design of the instrument and description of the retrieval algorithm can be found in Straub et al. (2010) and Tschanz et al. (2013).

2.3 Aura-MLS

The Microwave Limb Sounder (MLS) is one of the payloads onboard NASA's EOS-Aura satellite which was launched in 2004 (Waters et al., 2006). The satellite is in a Sun-synchronous orbital altitude of 705 km, with a period of 1.7 hours, and 98 °
115 inclination. MLS scans the limb in the direction of orbital motion which gives almost pole-to-pole coverage (82°S to 82°N) with each profile spaced 1.5 degrees or 165 km along the orbit track. Ozone is retrieved from the band of 240 GHz and water vapor from the 183 GHz line. Temperature is derived from radiances measured by the 118 GHz and 240 GHz radiometers with a vertical resolution of 3-6 km. MLS provides ozone profiles (version 5) from 12 to 80 km altitude with a vertical resolution of 2.5-6 km and water vapor profiles (version 5) from 10 to 90 km with a vertical resolution of 3.5 km from 316 to 4.64 hPa
120 and 15 km above 0.1 hPa. We extracted ozone (Schwartz et al., 2015a), water vapor (Lambert et al., 2015), and temperature (Schwartz et al., 2015b) observations at Ny-Ålesund. It passes at Ny-Ålesund two times a day at around 04:00 and 10:00 UTC. (Profiles for comparison are extracted if their location is within ±400 km latitude and ±800 km longitude from Ny-Ålesund and the defined virtual conjugate latitude station.

2.4 MERRA-2

125 The Modern-Era Retrospective Analysis for Research and Applications, version 2 (Waters et al., 2006; Gelaro et al., 2017, MERRA-2) is the latest global atmospheric reanalysis produced by the NASA Global Modeling and Assimilation Office (GMAO) from 1980 to the present. MERRA-2 assimilates observation types not available to its predecessor, MERRA, and includes updates to the Goddard Earth Observing System (GEOS) model and analysis scheme so as to provide a viable ongoing climate analysis beyond MERRA's terminus. MERRA-2 provides a regularly-gridded, homogeneous record of the global atmo-
130 sphere, and incorporates additional aspects of the climate system including several improvements to the trace gas constituents and land surface representation, and cryospheric processes. We use the ozone and water vapor with 72 hybrid-eta levels from

the surface up to 0.01 hPa and a horizontal resolution of $0.5° × 0.625°$. The time resolution is 6 hours. MERRA-2 products are accessible online through the NASA Goddard Earth Sciences Data Information Services Center (GES DISC).

3 Time series of ozone and water vapor

135 GROMOS-C and MIAWARA-C perform highly accurate continuous ozone and water vapor measurements which are, however, only available at single locations and, thus, are representative of a specific geographic location. Both instruments are located at Ny-Ålesund, Svalbard (79° N, 12° E) and gathered continuous measurements since September 2015. We use GROMOS-C and MIAWARA-C data combined with MERRA-2 reanalysis and Aura-MLS satellite data to present the time series of ozone and water over northern and southern polar stations. The corresponding virtual conjugate latitude station (79° S, 12° E) is shown
140 in Fig. 1.

3.1 Ny-Ålesund, Svalbard (79° N, 12° E) in the NH

The time series of daily ozone for GROMOS-C, MERRA-2, and Aura-MLS at Ny-Ålesund, Svalbard (79° N, 12° E) extending from 2015 to 2021 are shown in Fig. 2. The ozone daily profiles measured with GROMOS-C cover a pressure range of 100-0.03 hPa which corresponds to about 16-70 km. The horizontal upper and lower white lines indicate the bounds of the trustworthy
145 pressure range where the measurement response is larger than 0.8, meaning that the measured spectrum contributes more than 80% to the retrieved profile.

Fig. 2 reveals the annual ozone cycle with higher ozone VMR in summer (about 6 ppmv) than in winter (about 4.5 ppmv) at about 5 hPa ($≈35$ km). GROMOS-C ozone VMR time series together with MERRA-2 and Aura-MLS at about 5 hPa smoothed by a 30 -day running mean is shown in Fig. A1a. We can see that all three datasets are able to capture the ozone annual varia-
150 tions well in the stratosphere. Stratospheric ozone largely follows the annual cycle of solar irradiation and is produced through the Chapman cycle, in particular, ozone VMR is mainly dominated by photo-chemically production in the summer months in the Arctic middle atmosphere.

In late winter and spring, the stratospheric ozone's higher variability is largely associated with the stratospheric polar vortex. Fig. 2 presents the ozone VMR starts to increase up to the maximum value of about 8 ppmv for some of the years in the strato-
155 sphere when the polar vortex is disturbed or weakened by the planetary waves leading to the formation of sudden stratospheric warming events. It shows that the planetary wave activity results in meridional transport of the ozone-rich air from the subtropics towards the pole, and perturbed significantly the distribution of ozone. For example, the polar vortex split and shifted away from Ny-Ålesund, ozone VMR reached about 7 ppmv during the winter 2018/2019 sudden stratospheric warming (Schranz et al., 2020). In some years, the polar vortex is stable and strong over Ny-Ålesund, and ozone VMR sustains smaller values. At
160 the end of the winter 2019/2020 season, the stratosphere featured an extremely strong and cold polar vortex resulting in low stratospheric ozone in the polar regions (Lawrence et al., 2020b; Inness et al., 2020). During late summer and early autumn, stratospheric ozone decreases rapidly when the vortex passes over Ny-Ålesund.

GROMOS-C and Aura-MLS present the secondary ozone layer at 0.03 hPa ($≈70$ km) in winter months but the very big values

above 0.1 hPa in MERRA-2 (as shown in the red shading in Fig. 2b). Wargan et al. (2017) identified that ozone in MERRA-2
165 data was expected to have higher uncertainties in the polar regions due to the higher dynamic variability in the areas. The alter-
ation of dynamical processes causes dramatic variability in trace gas concentrations in the middle atmosphere. The complexity
of altered dynamics might introduce extra uncertainties into numerical models and data assimilation systems. Therefore, the
red shading in Fig. 2b is related to model ozone biases in MERRA-2 due to mesospheric parameterization being disabled in
the NASA Goddard Earth Observing System Composition Forecast (GEOS-CF) and stratospheric chemistry now extends up
170 through the top of the GEOS atmosphere, thus avoiding the need to repeatedly read in production and loss rates (Knowland
et al., 2022). However, in this study, we focus on the stratospheric ozone in MERRA-2 reanalysis data and will not emphasize
altitudes indicating these biases. Remarkably, Fig. 2 shows the consistencies between GROMOS-C, MERRA-2, and Aura-MLS
time series of ozone VMR and highlights the good qualitative agreement of GROMOS-C with both datasets for the period. In
the stratosphere, a clear annual cycle is well captured by all datasets, and the higher variability of ozone in winter and spring
175 seasons is clearly visible.
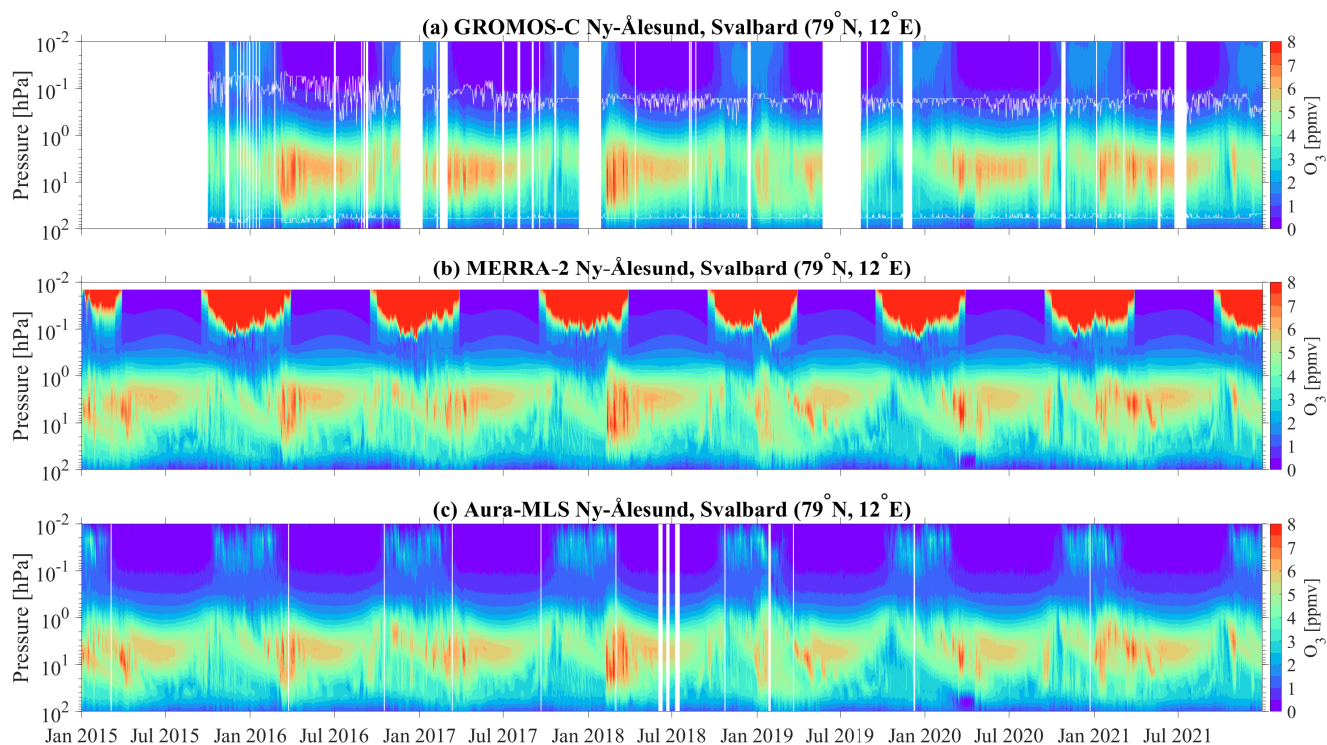
Figure 2. Time series of daily ozone VMR as a function of pressure over Ny-Ålesund, Svalbard (79° N, 12° E) for the 2015-2021 period.
Panels show ozone VMR from (a) GROMOS-C measurements, (b) MERRA-2 reanalysis data, and (c) MLS satellite observations. The
vertical white lines represent the data gaps caused by the hardware and measurement problems. The horizontal upper and lower white lines
indicate a measurement response of 0.8 in Fig. 2a.

Fig. 3 shows the time series of daily water vapor VMR from MIAWARA-C, MERRA-2, and Aura-MLS at Ny-Ålesund, Svalbard (79° N, 12° E) for the period 2015-2021. MIAWARA-C measures continuously water vapor profiles which cover a pressure range from 5-0.02 hPa corresponding to about 37-75 km. The horizontal upper and lower white lines indicate again the bounds of the trustworthy pressure range where the measurement response is larger than 0.8.

The most evident feature of water vapor is its annual cycle with higher mixing ratios during local summertime and lower mixing ratios during local wintertime throughout the middle atmosphere. This seasonal behavior is mainly driven by the upward and downward branches of the mesospheric residual circulation. As shown in Fig. A1a, water vapor VMR has a maximum of about 7.5 ppmv in summer and a minimum of about 3.5 ppmv in winter at 0.1 hPa (approximately 60 km). Due to the air subsidence inside the polar vortex from autumn to winter, water vapor VMR reaches the maximum at 10 hPa.

In some years, water vapor exhibits a larger variability in late winter and spring. The variation of water vapor is mainly affected by the occurrence of a major SSW which interrupts the polar vortex, after that, the vortex recovers, and the lower mesospheric water vapor content increases and is accompanied by a decrease in the stratosphere, corresponding to the water vapor vertical profile in the regions outside of the polar vortex (Schranz et al., 2019, 2020). In general, MIAWARA-C captured the annually varying mesospheric distribution of water vapor agrees well with reanalysis data and satellite observations. However, there are notable differences at the polar latitudes in the water vapor VMR compared to MERRA-2 throughout the stratosphere and the mesosphere. MERRA2 shows a tendency to lower water vapor VMR compared to MIAWARA-C and MLS observations. This is likely related to the lack of assimilated observations and known deficiencies in the representation of stratospheric transport (Davis et al., 2017) in the reanalysis data.
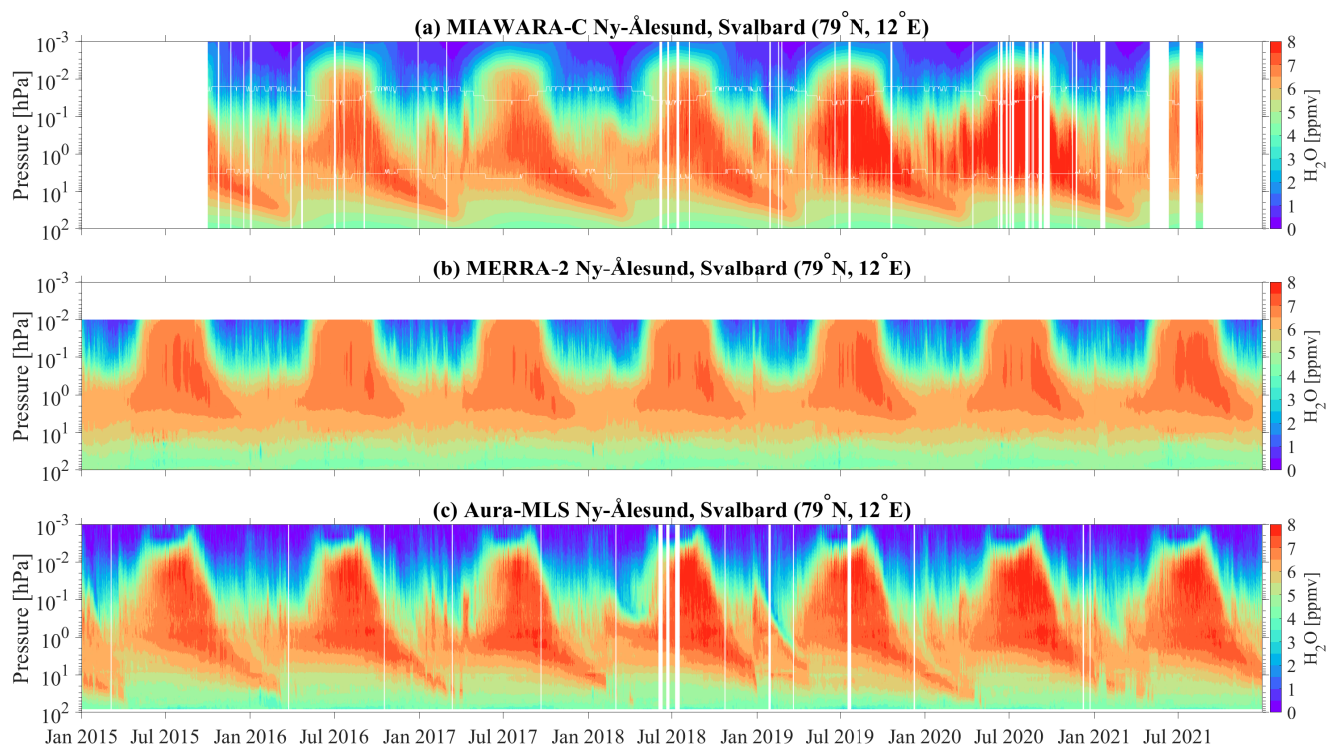
Figure 3. Time series of water vapor VMR as a function of pressure over Ny-Ålesund, Svalbard (79° N, 12° E) for the 2015-2021 period. Panels show ozone VMR from (a) MIAWARA-C measurements, (b) MERRA-2 reanalysis, and (c) MLS satellite observations. The vertical white lines represent the data gaps caused by the hardware and measurement problems. The horizontal upper and lower white lines indicate a measurement response of 0.8 in Fig. 3a.

3.2 Conjugate latitude station (79° S, 12° E) in the SH

Fig. 4 and Fig. 5 show time series of ozone and water vapor VMR from MERRA-2 and Aura-MLS at conjugate latitude station (79° S, 12° E) for the 2015-2021 period, respectively. For comparison purposes, the conjugate latitude station results are lagged by 6 months relative to those for Ny-Ålesund. Both stations exhibit annual cycles of ozone while the conjugate latitude station shows an ozone VMR maximum of about 6 ppmv in winter and a minimum of about 4 ppmv in summer at about 5 hPa (Fig. A1b).

Compared to the interannual ozone variability at Ny-Ålesund, the results from the conjugate latitude station are less variable throughout the spring in the stratosphere. Compared to the NH, the planetary wave activity is much weaker in the SH where a minimum in the ozone mixing ratios prevails over the polar latitudes during the late winter and spring. There is a dominance of an isolated and stable polar vortex which inhibits the meridional ozone transport to the south pole throughout the annual cycle, and the formation of polar stratospheric clouds promotes the production of chemically active chlorine and bromine leading to catalytic ozone depletion in the lower stratosphere. This process is well-reflected in the observations and models for Septem-

ber/October at the conjugate latitude station.

Fig. 5 presents the water vapor annual cycle with higher mixing ratios during local wintertime and lower mixing ratios during
210   local summertime over the conjugate latitude station. Furthermore, polar stratospheric cloud particles can sediment with considerable velocities and irreversibly remove water and nitric acid from the upper atmosphere resulting in a substantial reduction of water vapor VMR at the lower stratosphere during the southern polar winter and early spring (Waibel et al., 1999; Tritscher et al., 2021). After September, the water vapor VMR increases again as the polar stratospheric cloud influence reduces.
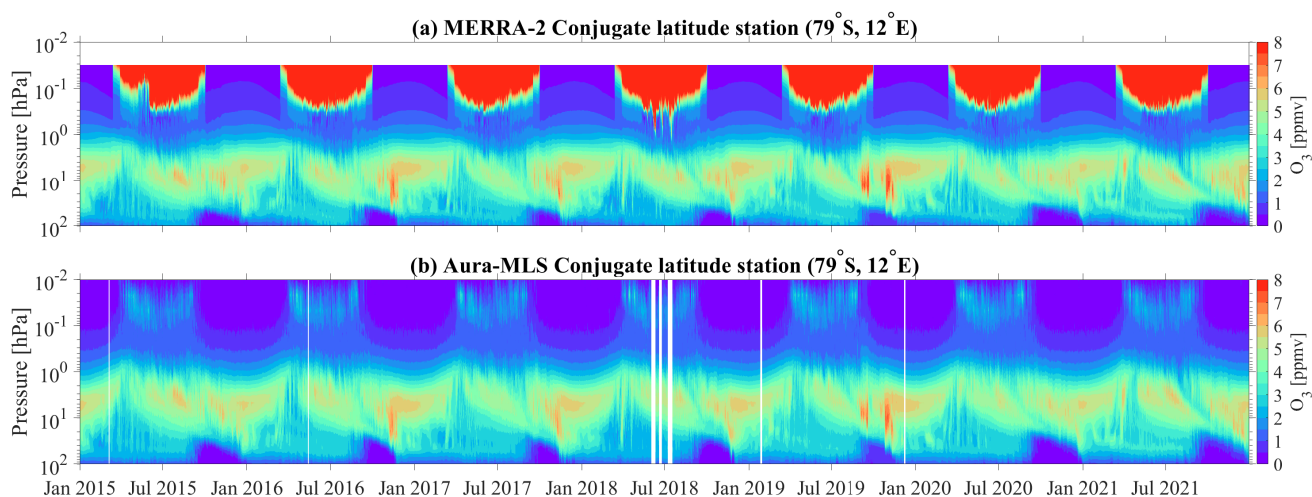
Figure 4. Same as Fig. 2 (without GROMOS-C measurements) but for the SH at conjugate latitude station (79° S, 12° E).
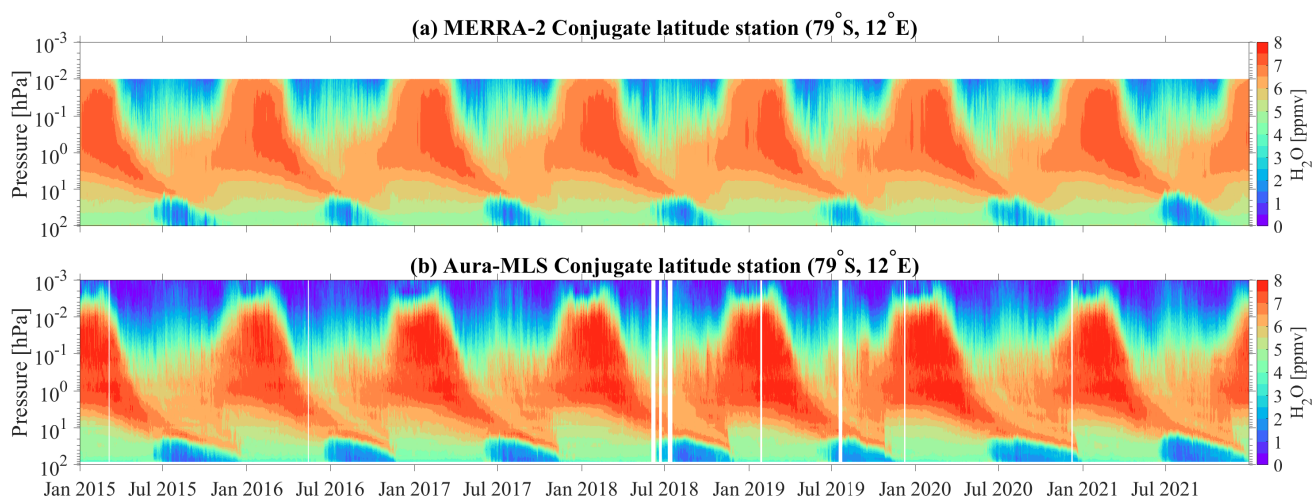
Figure 5. Same as Fig. 3 (without MIAWARA-C measurements) but for the SH at conjugate latitude station (79° S, 12° E).

4 Climatologies of ozone and water vapor

215 This section examines the ozone and water vapor climatologies over Ny-Ålesund, Svalbard (79° N, 12° E) and conjugate latitude station (79° S, 12° E) generated from GROMOS-C, MIAWARA-C, MERRA-2, and Aura-MLS datasets. It is important to evaluate how well GROMOS-C and MIAWARA-C can monitor the ozone and water vapor variability and characterize their distribution in the Arctic middle atmosphere.

4.1 Ozone

220 Figure. 6 shows the climatological ozone distribution as a function of pressure and time deduced from GROMOS-C, MERRA-2, and Aura-MLS in both hemispheres. Many features of ozone microwave radiometer measurement climatologies are broadly consistent with model and satellite data. Some exceptionally maximum values larger than 8 ppmv in MERRA-2 data above 0.1 hPa are described in section 3.

Overall, the ozone profile reveals a characteristic seasonal dependence at polar latitudes. In particular, the altitude of the
225 maximum ozone VMR as well as its temporal variability exhibits a seasonality. The peak ozone VMR (approximately 6.5 ppmv) appears in the NH in the late spring, whereas autumn shows the lowest values throughout the course of the year. The maximum observed and modeled in the SH (approximately 5.5 ppmv) is somewhat smaller and earlier in the season compared to the maximum occurring in the northern hemisphere. The primary driver of the hemispheric maximum in ozone VMR is related to circulation processes throughout the stratosphere, including those associated with the Brewer–Dobson circulation,
230 transporting ozone-rich air toward the poles in the winter-spring hemisphere. Precisely, this circulation moves the ozone-rich air from the tropical photochemical source region to high latitude after the polar vortex broke down and essentially enables the intrusion of ozone rich-air from the mid-latitudes into the polar cap and replacement of the ozone-depleted air masses.

MERRA-2 and MLS capture well the ozone hole in the polar lower stratosphere from September to November in the SH. However, the climatology of ozone in the NH does not reflect a corresponding signature. The annual cycle of ozone at 46 hPa
235 in both hemispheres further reveals this significant feature as shown in Fig. 7. The northern hemispheric annual cycle of ozone at 3 hPa peaks in March and reaches a minimum in October. The SH reaches two minimum values in April and August and peaks in the summer and winter. Both hemispheres have dramatically different seasonal variations and distribution in ozone due to differences in the stratospheric dynamics of the two hemispheres. Another essential feature is that the ozone secondary maximum in the polar regions is captured by GROMOS-C and Aura-MLS in the early winter in the NH, and appears in late
240 spring at the mesosphere (about 0.03 hPa) in the SH.
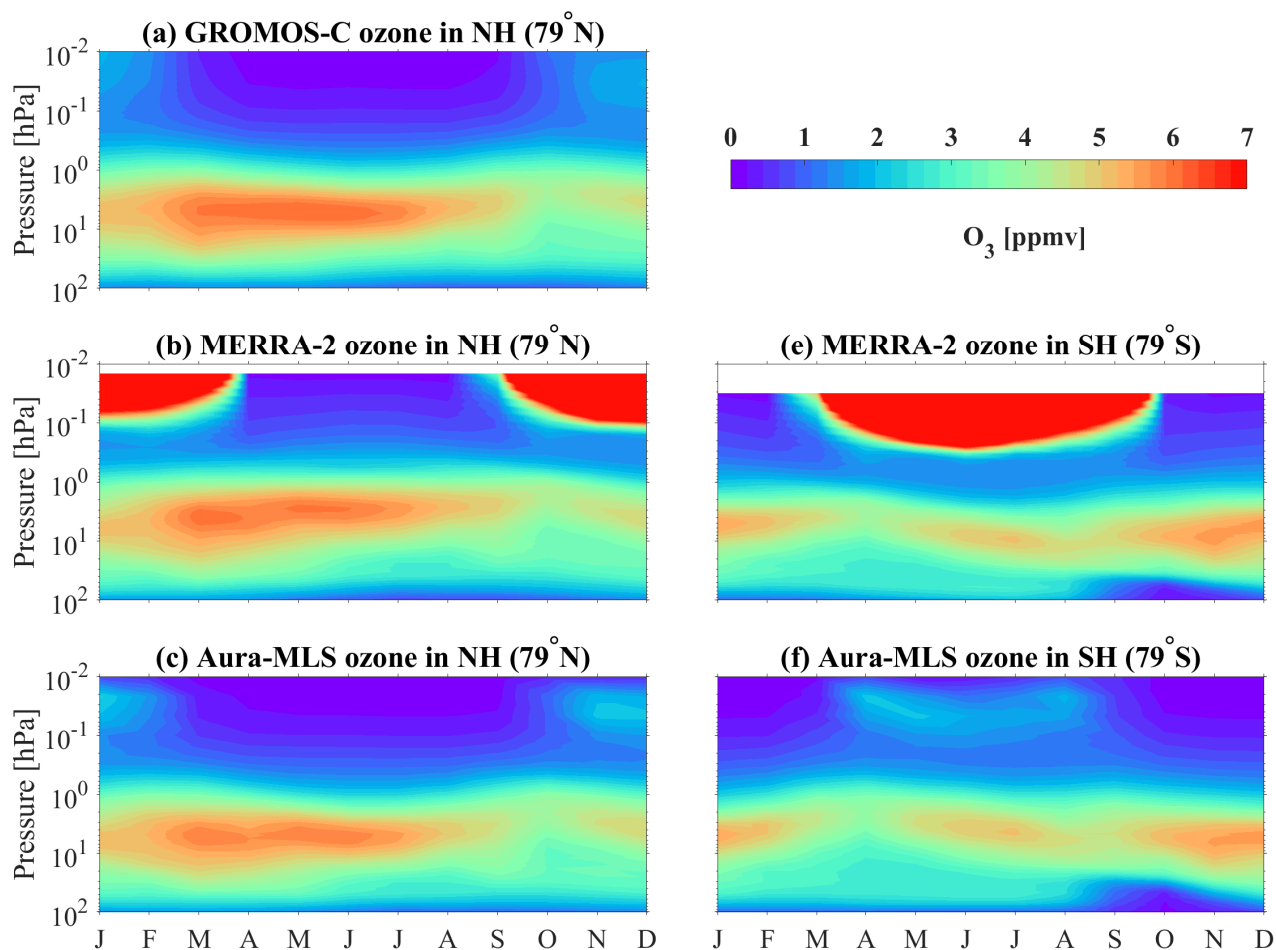
Figure 6. Climatology (2015-2021) of the ozone monthly distribution from GROMOS-C (a), MERRA-2 (b, e), and Aura-MLS(c, f) above Ny-Ålesund, Svalbard in the NH and conjugate latitude station in the SH. There is no GROMOS-C measurement for ozone in the SH. The x-axis is the month.
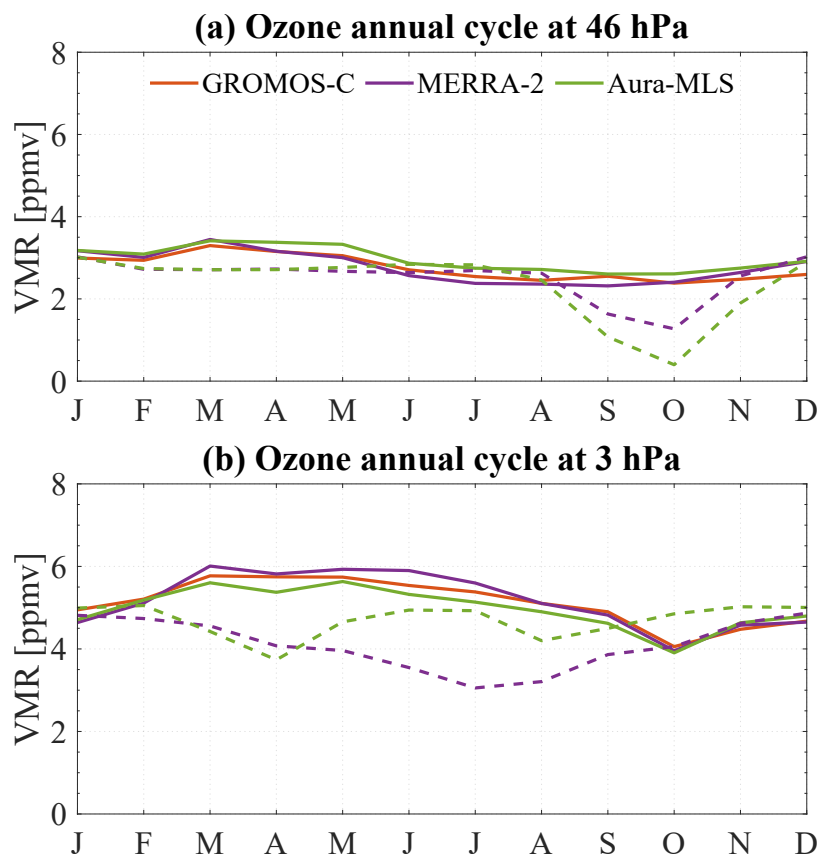
Figure 7. The annual cycles of monthly ozone VMR from GROMOS-C, MERRA-2, and Aura-MLS at 46 hPa (a) and 3 hPa (b). Solid lines represent Ny-Ålesund in NH and dashed lines represent conjugate latitude station in SH. Each month is averaged for the years 2015-2021.

4.2 Water vapor

Fig. 8 shows the climatology of water vapor vertical and temporal distribution from MIAWARA-C, MERRA-2, and Aura-MLS over both stations (79° S and 79° N) compiled from measurements collected between 2015 and 2021. The annual variation of water vapor with a maximum during hemispheric summer and a minimum during hemispheric winter is clearly visible. During the hemispheric winter, the middle atmospheric water vapor maximum is shifted down to about 10 hPa while it rises up to the lower mesosphere during the hemispheric summer. The characteristics of water vapor in both hemispheres depend strongly on the mesospheric pole-to-pole circulation which is an upwelling with moist air transporting upwards for the hemispheric summer and a corresponding downward motion with dry air into the stratosphere during the winter (Orsolini et al., 2010). In addition, due to the relatively long photo-chemical lifetime of water vapor, more water vapor produced by methane oxidation accumulates in summer.

The annual cycle of monthly water vapor VMR at three separate pressure levels (3, 0.3, and 0.02 hPa) in both hemispheres can be seen in Fig. 9. Water vapor VMR appears at a maximum in October in NH (April in SH) in the stratosphere (3 hPa) due

to the oxidation of methane. Due to photodissociation caused by Solar Lyman-α radiation acting as a sink and the amount of water vapor being in equilibrium between different photochemical processes and vertical transport, water vapor is more smooth

255 with nearly constant mixing ratios from winter to spring in the NH (from late summer to autumn in the SH). In the mesosphere (0.3 and 0.02 hPa), water vapor gradient variations can be found during hemispheric spring and summer. The gradient at 0.02 hPa is steeper than at 0.3 hPa from April to July in NH (from November to January in SH). Furthermore, the positive gradient is weaker but the time of increase lasts longer and shows an extreme negative gradient in the hemispheric autumn. In both hemispheres, the seasonal behavior of water vapor is almost symmetric at 0.02 hPa and has a slight asymmetry at 0.3 hPa. At

260 0.02 hPa the maximum value of the water vapor mixing ratio persists for one month long and at 0.3 hPa the decrease in water vapor is not visible until September in the NH (March in the SH), however then with a steep gradient.
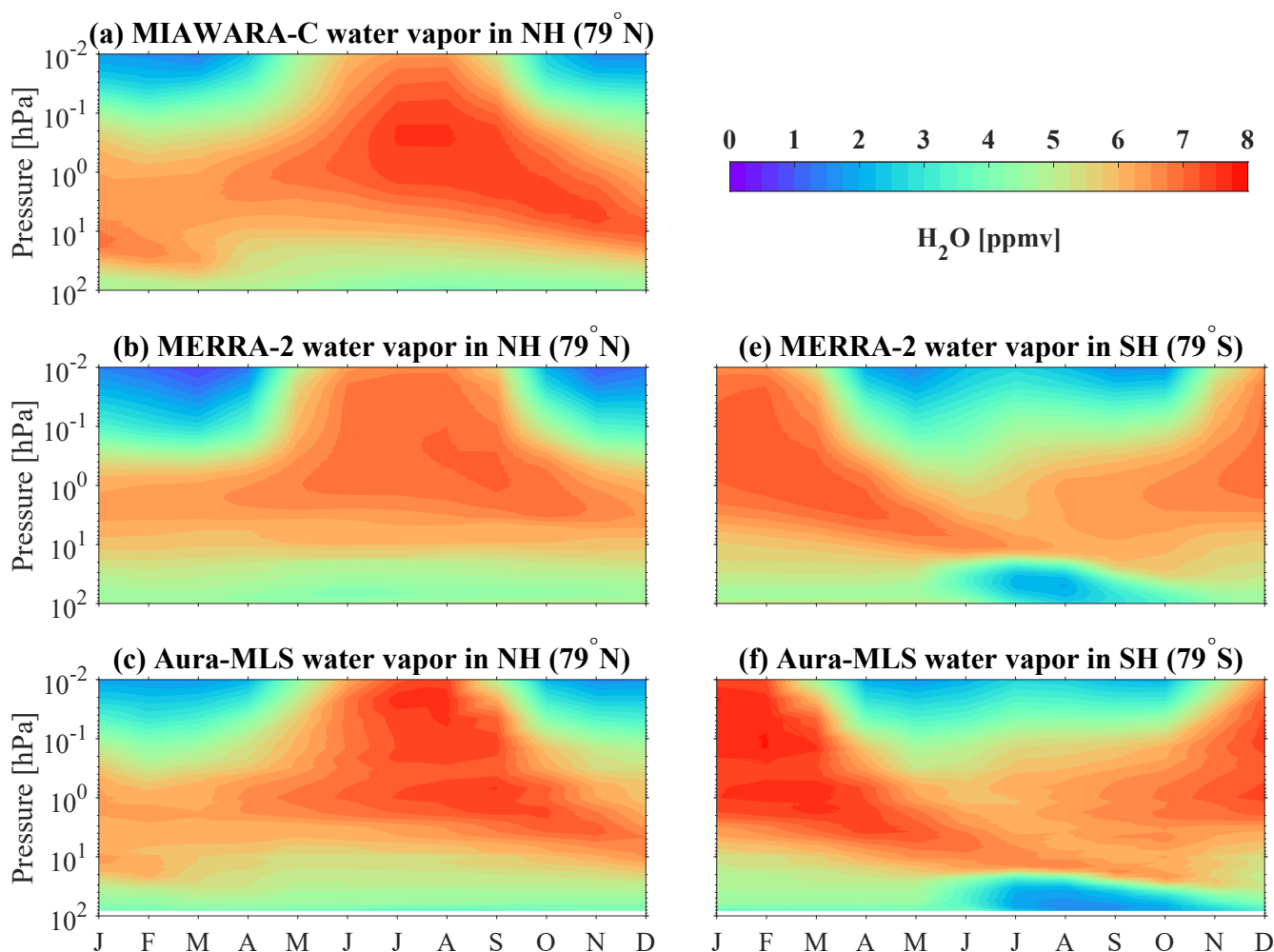
Figure 8. Climatology (2015-2021) of the water vapor monthly distribution from MIAWARA-C (a), MERRA-2 (b, e), and Aura-MLS(c, f) above Ny-Ålesund, Svalbard in NH and conjugate latitude station in SH. There is no MIAWARA-C measurement for water vapor in SH.
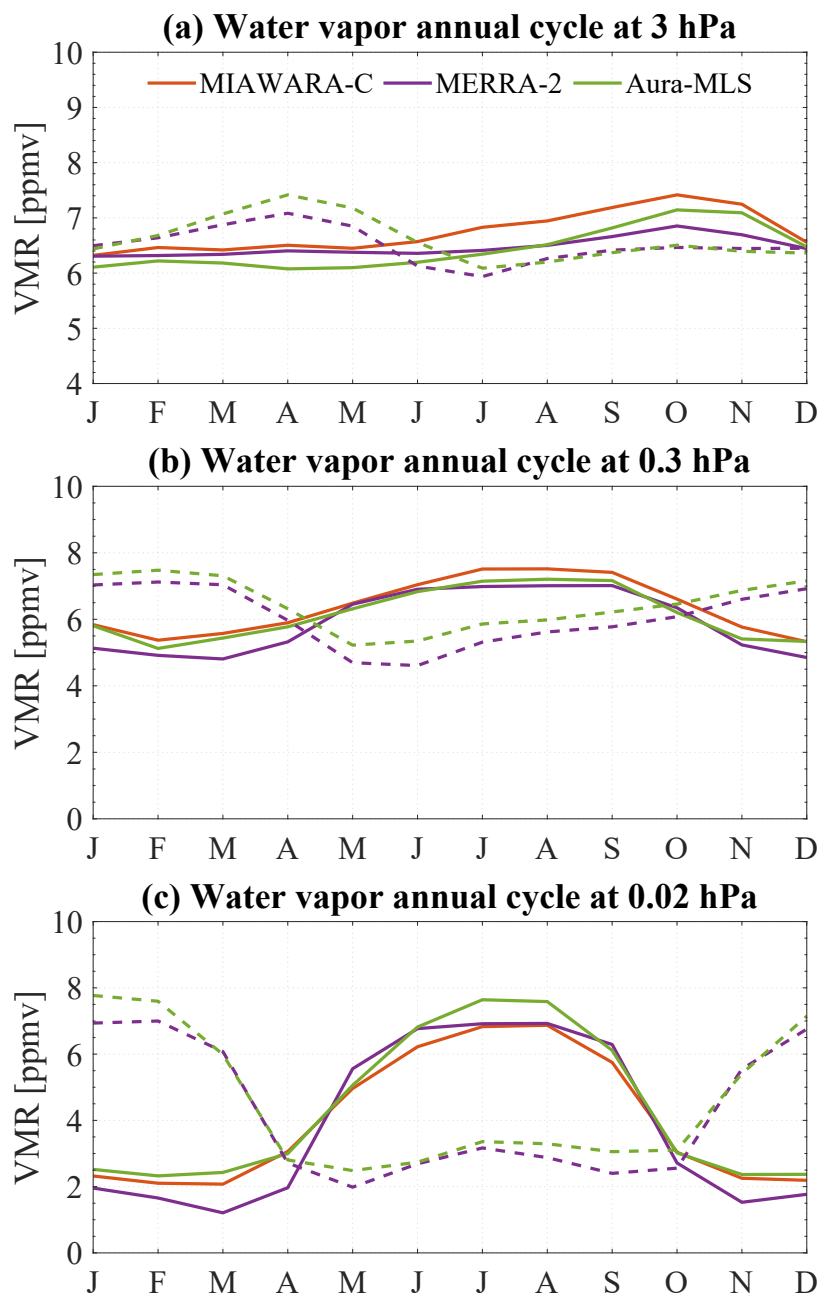
Figure 9. The annual cycles of monthly ozone VMR from GROMOS-C, MERRA-2, and Aura-MLS at 3 hPa (a), 0.3 hPa (b), and 0.02 hPa (c). Solid lines represent Ny-Ålesund in NH and dashed lines represent conjugate latitude station in SH. Each month is averaged for the years 2015-2021.

4.3 Relative differences

In the two ground-based radiometer measurements from GROMOS-C and MIAWARA-C, the aforementioned seasonal be-
265 havior in their ozone and water vapor distributions display very similar patterns to Aura-MLS and MERRA-2. Still, there are
distinct differences between the datasets. To quantitatively assess the consistency of the ozone and water vapor climatologies
from GROMOS-C and MIAWARA-C, the relative differences (RDs) of ozone and water vapor VMR between the ground-based
microwave radiometers and the two other data sets are calculated using the expression:

$$RD = \frac{(\varphi)_{radiometer} - (\varphi)_{dataset}}{(\varphi)_{dataset}} \cdot 100\% \tag{1}$$

270 Where φ represents either ozone or water vapor VMR. Fig. 10 shows the relative differences of ozone and water vapor clima-
tologies from GROMOS-C and MIAWARA-C, respectively, with respect to MERRA-2 and Aura-MLS. In Fig. 10, obviously,
the largest negative RD is larger than 50% above 0.2 hPa because of the mesospheric ozone parameterization being disabled in
MERRA-2 (Knowland et al., 2022). The RD between GROMOS-C and MERRA-2 is above 30% in summer and within 10%
in winter at the pressure range of 30-10 hPa. GROMOS-C and Aura-MLS agree well in most of the stratosphere, with RDs
275 mainly within ±10%, but include the RDs greater than ±15% in the lower mesosphere.
The RD between MIAWARA-C and MERRA-2 is larger than 50% throughout the late autumn to spring months above 0.2 hPa
because of the lack of observational data on the assimilation of water vapor in the polar mesosphere (Davis et al., 2017). Addi-
tionally, the RDs mainly within 10% in the upper stratosphere and lower mesosphere (about 10–0.3 hPa) indicate MIAWARA-
C performs quite well as compared to the MERRA-2 reanalysis data. MIAWARA-C and Aura-MLS show relatively good
280 agreement, with RDs within ±5% throughout the upper stratosphere and mesosphere (about 5–0.02 hPa). Note that the RDs
between ground-based microwave radiometers and Aura-MLS likely result from the Aura-MLS extracting method (as men-
tioned in Sect. 2) which leads to changes in the polar ozone and water vapor distribution. Furthermore, the diurnal cycle in the
ozone and water vapor has not been explicitly accounted for in the GROMOS-C and MIAWARA-C measurements. Neglecting
the diurnal cycle potentially contributes to differences between microwave radiometer measurement and other data sets.
285 Overall, GROMOS-C and MIAWARA-C are valuable to monitor the distribution of stratospheric ozone and mesospheric water
vapor at the polar latitudes, respectively, which gives us more details to investigate their long-term variability, sources, and
trend.
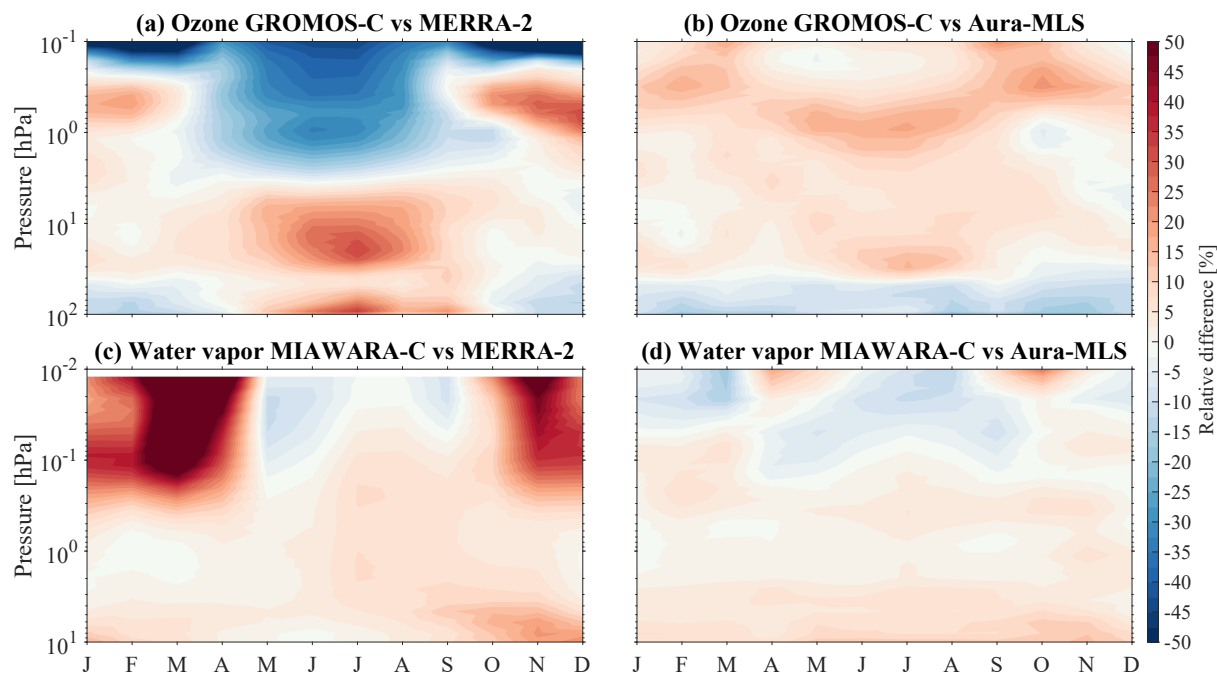
Figure 10. Monthly distributions of ozone and water vapor relative differences between ground-based microwave radiometers and data sets (a, c) MERRA-2, (b, d) Aura-MLS.

5   Dynamics and transport of water vapor

Water vapor is widely used as a tracer to investigate the dynamics of transport processes in the Arctic middle atmosphere
290   (Lossow et al., 2009; Straub et al., 2012; Tschanz et al., 2013; Schranz et al., 2019, 2020). The chemical lifetime of water vapor is of the order of years in the lower stratosphere, months in the lower mesosphere, and weeks in the upper mesosphere (Brasseur and Solomon, 2005). Water vapor mixing ratios display different dynamical features depending on the altitude ranges because of different vertical gradients of water vapor VMR above and below its peak in the upper stratosphere. The water vapor mixing ratio is assumed to be constant for one month and a half, and the vertical velocity of air can be estimated.
295   The time periods of the year when water vapor VMR increases and decreases with altitude (in the upper stratosphere and lower mesosphere) measured from MIAWARA-C and Aura-MLS over both Ny-Ålesund and conjugate latitude stations are well given in this study. We will denote the period with a stable high water vapor mixing ratio as the hemispheric summer and the positive and negative transition periods as the upwelling and downwelling branches, respectively. With the northern and southern hemispheric water vapor measurements, we calculate the effective ascent and descent rates as derived from a linear
300   regression fit to different water vapor mixing ratio isopleths (6.5 ppmv water vapor isopleth in Fig. 11 and Fig. 12).

The time period of 7 years of descent rate from 15 September to 31 October in the altitude range of about 50-70 km is well presented in Fig. 11 (the first and third rows). This is an estimated result not a quantitative calculation of the water vapor descent since the dynamic and chemical not directly related to descent may also affect the polar water vapor changes. However, the

effect of dynamic processes such as planetary wave disturbance is relatively obvious to estimate the ascent rate. As shown in Fig. 11 (second and fourth rows), the time period of five years (2015, 2016, 2017, 2018, and 2021) of ascent rate starts from 05 May to 20 June and another two years (2019 and 2020) the starting time for the increase of water vapor happens earlier by approximately 20 days which is from 15 April. MIAWARA-C and Aura-MLS observe in 2019 and 2020 years the return of the water vapor mixing ratio to pre-winter values in mid-April and the moist air is lifted to greater altitudes in early May. The starting time of the ascent rate in 2019 and 2020 is slightly earlier than that in other years, which is the result of several processes. The planetary waves displace the polar vortex above Ny-Ålesund, and water vapor-rich air is transported into the upper stratosphere, and furthermore, the maximum water vapor mixing ratio at the altitude of about 55 km is re-established. Wave breaking and mixing above the strongest vortex level tends to reduce the tracer gradient (Lee et al., 2011), leading to an increase in the water vapor mixing ratios. In addition, photochemical processes from solar radiation also can contribute to the accumulation of water vapor in the springtime at the stratopause altitude (Brasseur and Solomon, 2005).

In the SH, the time period of each year of the ascent rate is relatively consistent from 15 October to 30 November in the upper stratosphere and mesosphere (Fig. 12). The descent rate of water vapor from 15 March to 30 April in the SH appears to be similar for the 7 years, likely due to the higher stability and stronger of the southern polar vortex.
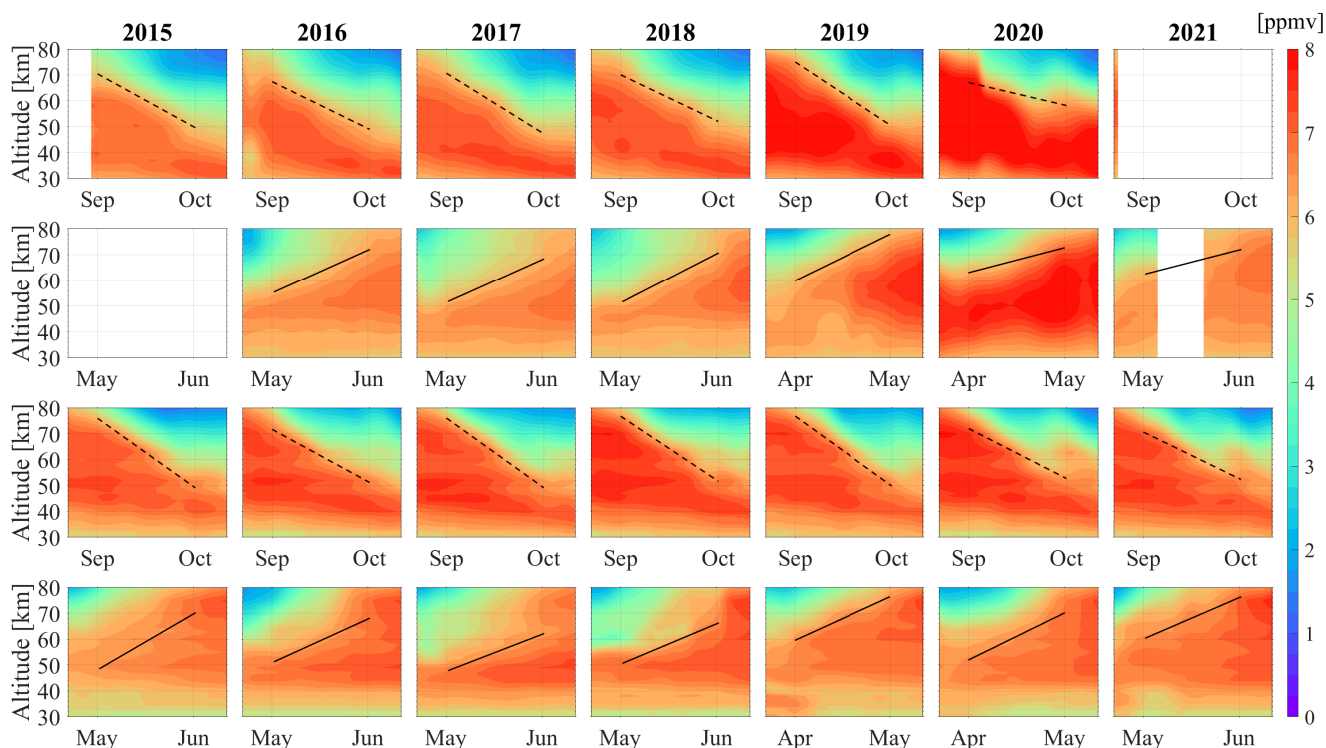
Figure 11. Time-altitude of mean water vapor VMR from MIAWARA-C (first and second rows) and Aura-MLS (third and fourth rows) over Ny-Ålesund, Svalbard (79°N, 12°E) in the NH. The data has been smoothed by a 20-day Gaussian. The black dashed and solid lines indicate the descent and ascent rates of water vapor as derived from a linear regression fit to the 6.5 ppmv isopleth of water vapor VMR, respectively. There is no data for MIAWARA-C from May to June 2015 and from September to October 2021.
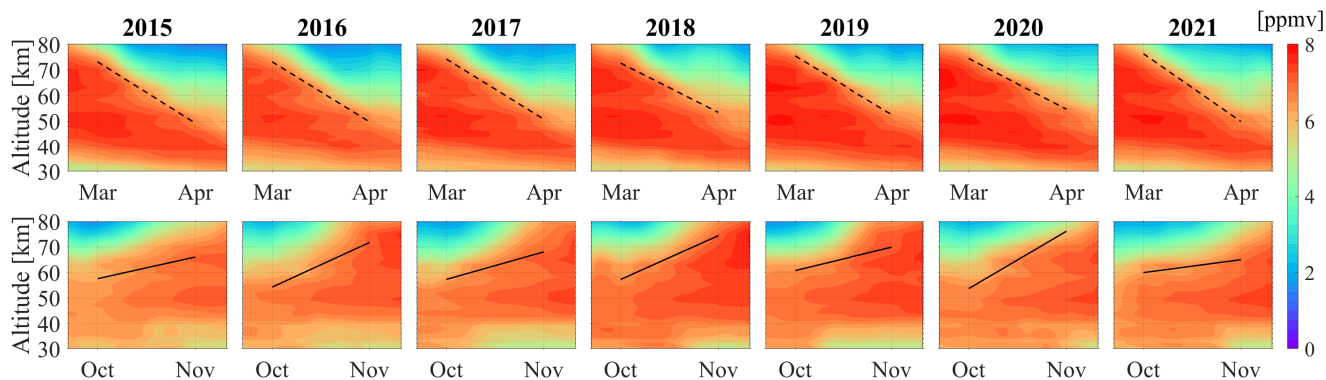
Figure 12. Same as Fig. 11 (without GROMOS-C measurements) but for conjugate latitude station (79° S, 12° E) in the SH.

Fig 13 shows the annual variability of effective ascent and descent rates in the southern and northern hemispheres during a given time period. In contrast to the NH, the southern hemispheric rate exhibit less interannual variability and an approximately

320   consistent variation with the rates corresponding to the different isopleths, which illustrate the qualitative agreement in different years in the effective vertical rates for the transition periods in the SH. Table 1 gives a more quantitative perspective to compare the vertical movement of air in both hemispheres. In the NH, the average vertical velocities are 3.42 ± 1.89 mm s^{-1} from MIAWARA-C and 4.64 ± 1.83 mm s^{-1} from Aura-MLS for upwelling from spring to summer, and 4.98 ± 1.08 mm s^{-1} from MIAWARA-C and 5.40 ± 1.54 mm s^{-1} from Aura-MLS for downwelling from summer to autumn. During the transition from

325   winter to spring, the vertical velocity is 5.22 ± 0.76 mm s^{-1} for downwelling and 2.61 ± 1.44 mm s^{-1} for upwelling from autumn to winter calculated by Aura-MLS in the SH. Table 1 shows a stronger upwelling branch in the NH polar summer mesosphere as compared to the SH, accompanied by a stronger downwelling branch towards the SH winter in the polar region. In general, these results assess the ability to derive middle atmospheric ascent and descent rates from water vapor measurements at polar latitudes and further provide evidence for the higher variability in the NH than in the SH.
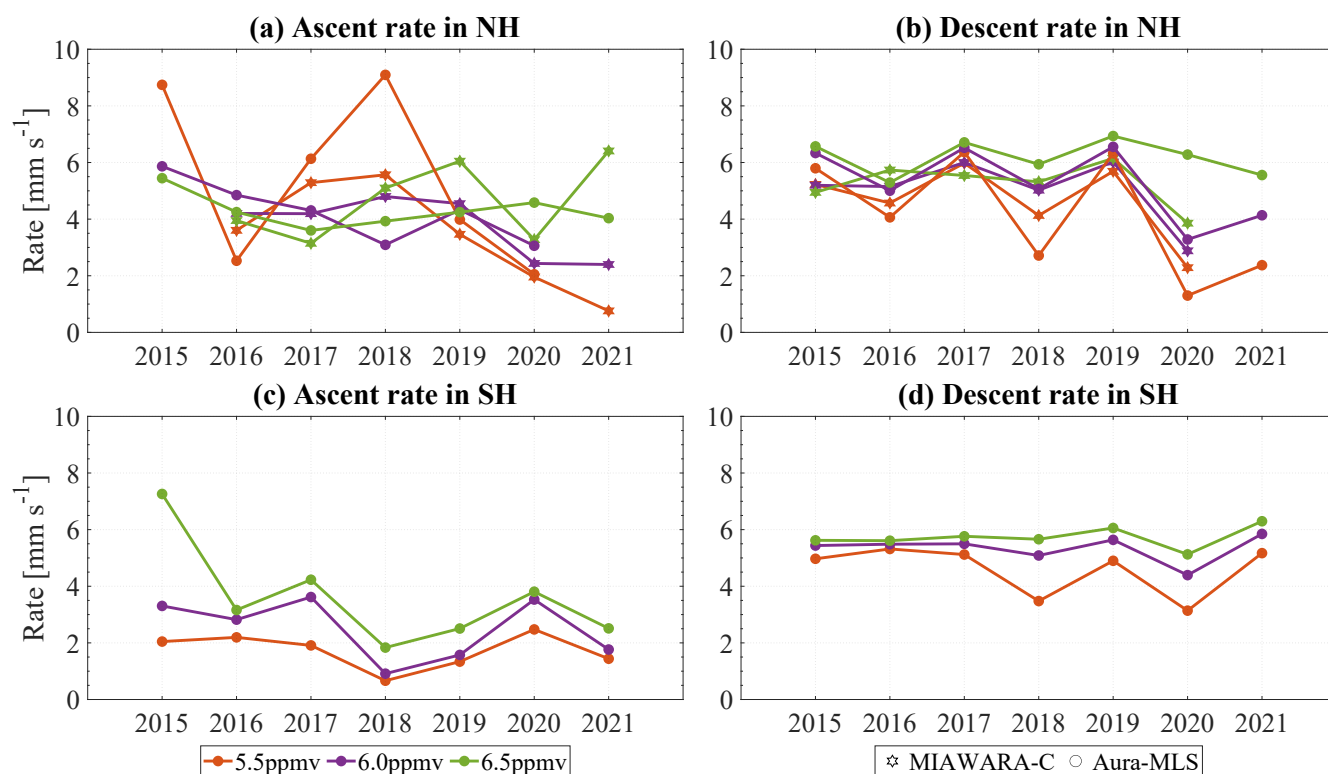
Figure 13. Interannual variability of the effective ascent and descent rates over both stations Ny-Ålesund, Svalbard (79°N, 12°E) and conjugate latitude station (79°S, 12°E) estimated from the linear regression fit to the 5.5, 6.0, and 6.5 ppmv isopleths of water vapor VMR from MIAWARA-C and Aura-MLS.

Table 1. Comparison of the mean values and standard deviations (SDs) of ascent and descent rates from MIAWARA-C and Aura-MLS in both hemispheres. The mean is computed for the rates from 5.5, 6.0, and 6.5 ppmv isopleths (as shown in Fig 13).

Ascent rate (mm s^{-1})	NH (mean±SD)	SH (mean±SD)
MIAWARA-C	3.42±1.89	-
Aura-MLS	4.64±1.83	2.61±1.44
Descent rate (mm s^{-1})	**NH (mean±SD)**	**SH (mean±SD)**
MIAWARA-C	4.98±1.08	-
Aura-MLS	5.40±1.54	5.22±0.76

6   Discussion

Continuous observations of essential climate variables such as ozone and water vapor are important for investigating the radiative balance of the atmosphere. Interhemispheric and interannual differences shed light on ozone and water vapor natural variability due to transport and photochemistry. Ground-based measurements such as those performed by GROMOS-C and MIAWARA-C permit to sustain of a high-resolution and continuous data set of these trace gases at remote locations such as Ny-Ålesund. A comparison to the Aura-MLS satellite data exhibits excellent agreement throughout all altitudes in the stratosphere to GROMOS-C, and the upper stratosphere and lower mesosphere to MIAWARA-C, respectively. The climatologies Aura-MLS and the microwave radiometers agree within ±10% during the year. However, a climatological comparison to the reanalysis data MERRA-2 and our ground-based radiometers indicates larger discrepancies above 0.2 hPa. These increased deviations are partially understandable by the implemented radiative transfer schemes and other model physics such as interactive chemistry, which is computationally much more expensive (Gelaro et al., 2017). Furthermore, MERRA-2 includes the MLS observations of temperature and ozone in the 3DVAR data assimilation (Wargan et al., 2017). MLS observations are most important for the mesosphere and are weighted by their precision and accuracy.

The interhemispheric comparison is performed by defining a virtual conjugate latitude station (79° S, 12° E) in the southern hemisphere at the conjugate geographic coordinates. Although the general seasonal morphology is very similar, the northern hemisphere shows much more variability in the time series of ozone and water vapor. One of the most significant differences is the occurrence of the ozone hole in the southern hemisphere towards the end of the winter season below 10 hPa (Solomon et al., 2014). During this time also the water vapor VMR measurements exhibit a minimum due to the formation of polar stratospheric clouds (Flury et al., 2009; Bazhenov, 2019) providing even more favorable conditions for catalytic ozone destruction reactions. In Fig 14, we present a conjugate latitude temperature comparison results between the polar and mid-latitudes from Aura-MLS observations in both hemispheres. The southern polar latitudes appear much colder than their northern counterparts (Fig B1). Furthermore, the temperature gradient between the mid- and high-latitudes is stronger in the southern hemisphere at the stratosphere and, thus, drives a more stable polar vortex due to the thermal wind balance, which prevents the mixing of

ozone-rich air from the low- and mid-latitude into the polar cap by planetary waves as it often can be observed in the northern hemisphere (Schranz et al., 2019). There are only a few occasions where in the northern hemisphere such a stable and cold polar vortex was observed (Matthias et al., 2016; Lawrence et al., 2020a), which also can lead to anomalies in the mesospheric dynamics (Stober et al., 2017).
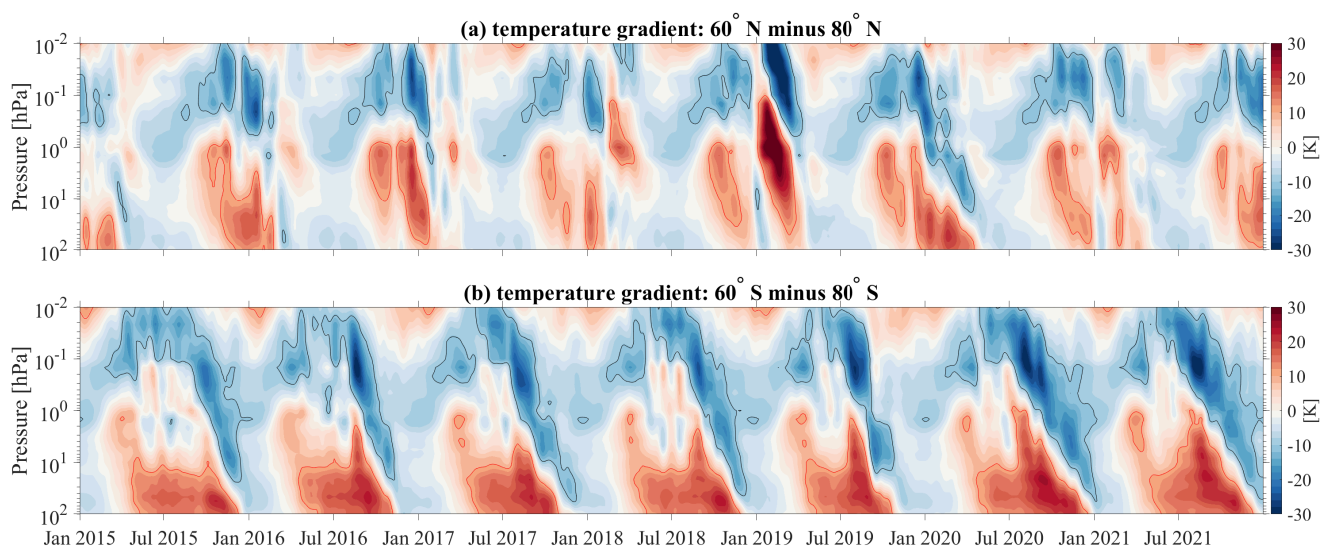
Figure 14. Temperature gradients between the mid-latitude and polar latitudes in the NH (60° N & 80° N) and SH (60° S & 80° S), respectively. Red and black contours represent positive and negative values (±10 K).

In addition to the strength of the polar vortex, we investigated the strength of the upwelling and downwelling in both hemispheres, which we consider a proxy of the strength of the residual circulation. Water vapor has a longer lifetime than CO at 50-70 km (Brasseur and Solomon, 2005), which makes it a more robust tracer to manifest the vertical motion of air. The effective rates of vertical transport are estimated by using the water vapor measurements following the approach presented by Straub et al. (2010). The vertical velocities are derived under the assumption that other processes such as chemical reactions, photodissociation, or horizontal advection are less important. Here we analyze periods around the equinoxes. During this time of the year, horizontal gradients between the polar region and the mid-latitudes are minimal or negligible and, thus, there is almost no meridional transport. Furthermore, we only investigated altitudes below typical OH-layer heights, which also reduces the impact of photodissociation in our estimates (Ryan et al., 2018). We obtained vertical velocities of 3.42 ± 1.89 and 4.64 ± 1.83 mm s^{-1} for the upwelling towards the northern hemispheric summer and vertical motions of 4.98 ± 1.08 and 5.40 ± 1.54 mm s^{-1} downwelling during the fall transition. Furthermore, there is rather significant interannual variability in the northern hemisphere that is not found above the Antarctic continent. Due to the frequent occurrence of sudden stratospheric warmings, the spring transition is more variable in the NH (Matthias et al., 2021). In the southern hemisphere, the spring transition towards summer is characterized by 2.61 ± 1.44 mm s^{-1} vertical velocity, and during the transition from summer to winter, the down-

welling with 5.22±0.76 mm s^{-1} vertical velocity is observed. This suggests that the interhemispheric coupling between the polar stratosphere and polar mesosphere (Körnich and Becker, 2010; Orsolini et al., 2010; Smith et al., 2020a) can explain the difference in interannual variability of upwelling and the corresponding downwelling in both hemispheres. Previous studies
375   investigating summer mesopause temperatures in the Northern hemisphere found a possible connection to the planetary wave activity at stratospheric altitudes in the southern hemisphere (Goldberg et al., 2004). Simulations with a gravity wave resolving model showed that the residual circulation and, thus, the gravity wave activity could be the mechanism that results in both an interhemispheric coupling (Becker and Fritts, 2006). Other observational studies using polar mesospheric clouds as well as stratospheric reanalysis data exhibited an interhemispheric correlation during the summer months (Karlsson et al., 2007).
380   Later, such a correlation was also found between mesospheric hydroxyl OH temperatures and stratospheric reanalysis (Espy et al., 2011). More recent model results suggested that the strongest interhemispheric coupling signatures are found between stratosphere and mesosphere in the opposite hemispheres (Smith et al., 2020b).

7   Conclusions

385   Continuous ground-based measurements of ozone and water vapor remain an essential tool to understand the short and long-term evolution of the middle atmosphere, as well as for the validation and parameterization of atmospheric models. In this study, we present ozone and water vapor measurements from the two ground-based radiometers GROMOS-C and MIAWARA-C located at Ny-Åesund, Svalbard collected between 2015 and 2021. The data were compared to observations from MLS onboard the AURA spacecraft as well as reanalysis data MERRA-2. This comparison showed a good agreement for the cli-
390   matological behavior between the ground-based radiometers and MLS to within almost ±10% for ozone at about 100–1 hPa, within ±5% for water vapor at about 5–0.02 hPa. However, we identified pronounced differences between the measurements and the reanalysis data above 0.2 hPa where MERRA-2 deviations up to 50% were visible. Ground-based observations are going to become more important within the next years as the satellite observations such as MLS are going to reach the end of their life and so far there are no adequate replacements in orbit.
395   By defining a virtual conjugate latitude station in the southern hemisphere, we investigated altitude-dependent interhemispheric differences. Both trace gases showed a much higher variability during the northern hemispheric winter driven by planetary wave activity. The southern hemisphere was characterized by a more stable polar vortex and colder temperatures in the polar cap that results in more favorable conditions to form polar stratospheric clouds and, thus, more efficient ozone destruction by catalytic reactions causing the well-known ozone hole. Furthermore, the polar stratospheric cloud formation was accompanied by a
400   reduction of the water vapor VMR at the same altitudes in the lower stratosphere.
We investigated the strength of the residual circulation by estimating the up- and downwelling above Ny-Åesund and the corresponding conjugate latitude station. Typical ascent rates during the summer transition reach values of 3.42-4.64 mm s^{-1} and for the downwelling, in the fall transition, vertical velocities of 4.98-5.40 mm s^{-1} are inferred. Correspondingly the vertical velocity of 2.46 mm s^{-1} for the upwelling and 5.22 mm s^{-1} for the downwelling is calculated in the SH. The northern hemi-

405 sphere also reflected a much more pronounced interannual variability compared to the southern polar latitudes. However, there is no strong correlation between up- and downwellings in the opposite hemispheres most likely due to dynamic processes such as the Quasi-Biennial Oscillation or weather patterns which play a role and need to be taken into account. Therefore, long-term ozone and water vapor measurements will improve a deeper understanding of the mechanisms which control polar ozone and water vapor variability and predict the future evolution of middle atmospheric ozone and water vapor in climate changes.

410 *Data availability.* The GROMOS-C and MIAWARA-C level 2 data are provided by the Network for the Detection of Atmospheric Composition Change and are available at http://www.ndacc.org (NDACC, 2022). MLS v5 data are available from the NASA Goddard Space Flight Center Earth Sciences Data and Information Services Center (GES DISC): https://doi.org/10.5067/Aura/MLS/DATA2516. MERRA-2 data are provided by NASA at the Modeling and Assimilation Data and Information Services Center (MDISC) and are available at the model level (GMAO, 2015a) at https://doi.org/10.5067/WWQSXQ8IVFW8 and in pressure level (GMAO, 2015b) at https://doi.org/10.5067/
415 QBZ6MG944HW0.

Competing interests. The contact author has declared that none of the authors has any competing interests.

Appendix A: Ozone and water vapor
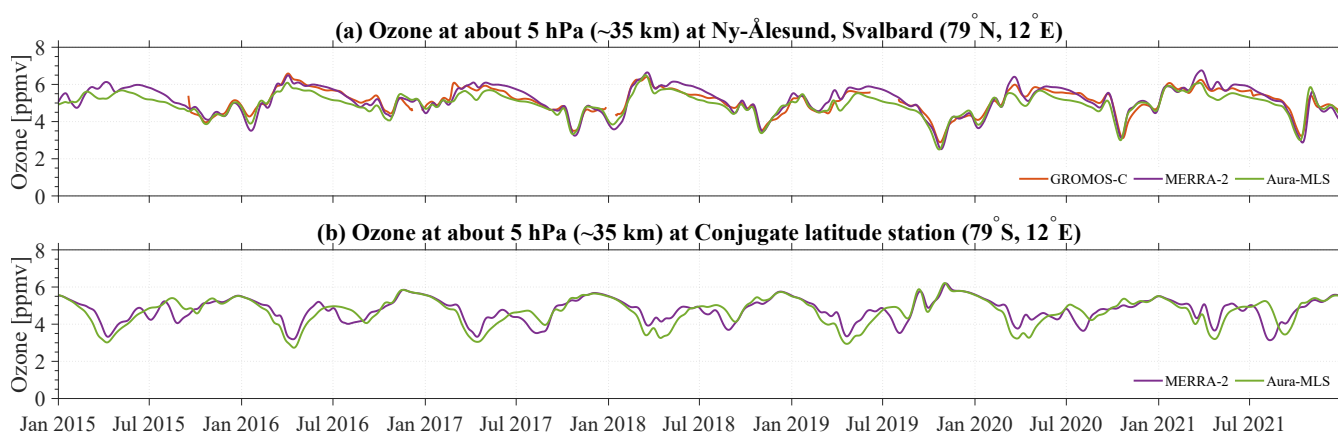
Figure A1. GROMOS-C, MERRA-2, and Aura-MLS ozone VMR time series at about 5 hPa smoothed by a 30-day running mean over Ny-Ålesund, Svalbard (79° N, 12° E) and conjugate latitude station (79° S, 12° E).
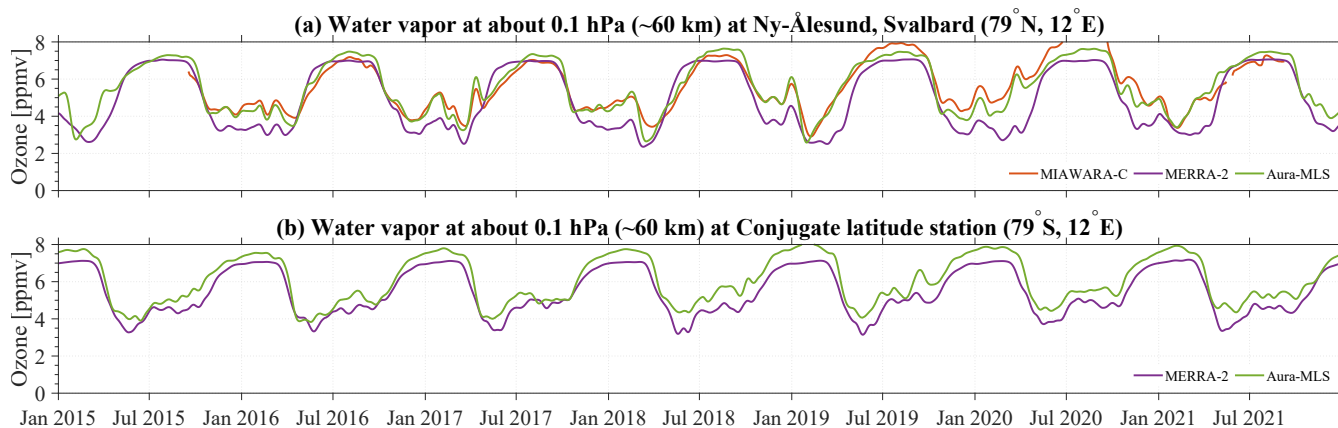
Figure A2. MIAWARA-C, MERRA-2, and Aura-MLS water vapor VMR time series at 0.1 hPa smoothed by a 30-day running mean over Ny-Ålesund, Svalbard (79° N, 12° E) and conjugate latitude station (79° S, 12° E).

Appendix B: Time series of temperature at the mid and polar latitudes
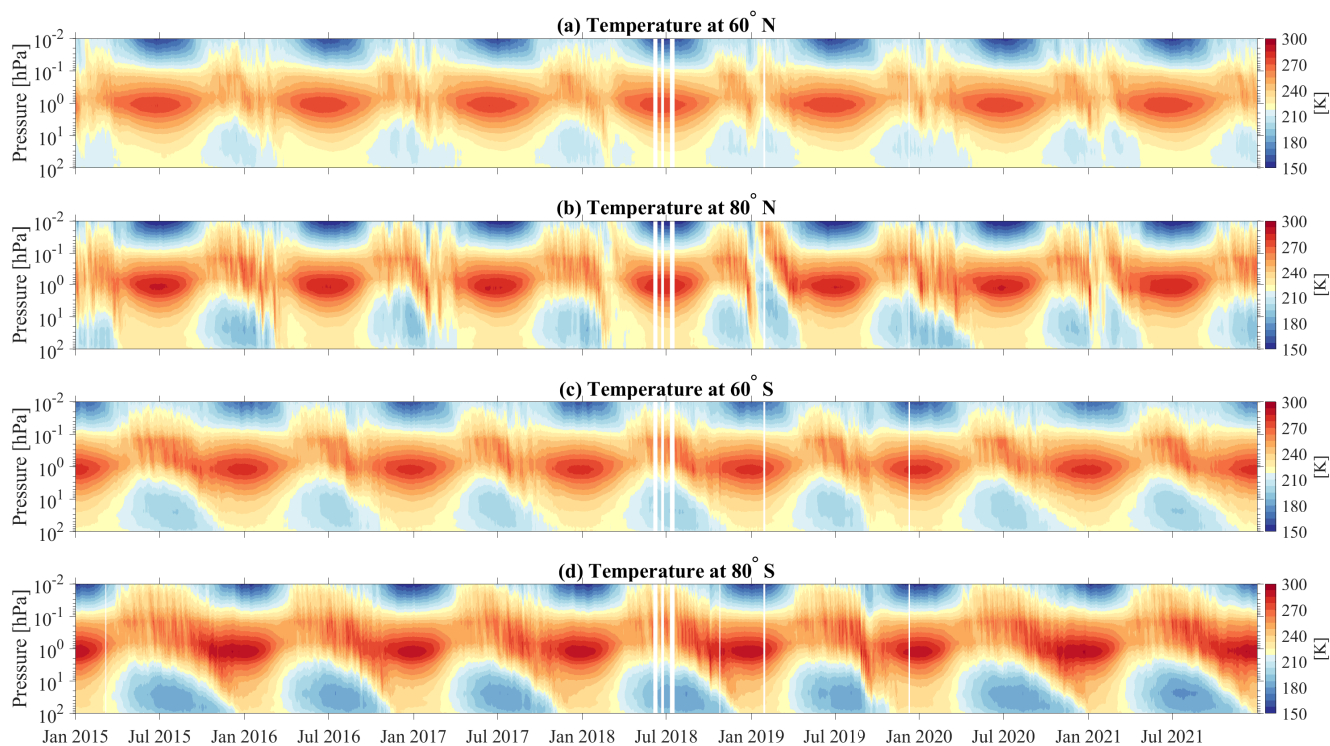
Figure B1. Time series of temperature from Aura-MLS observations as a function of pressure over conjugate polar latitudes (80° N & 80° S) and conjugate mid-latitudes (60° N & 60° S) in both hemispheres.

Author contributions. GS was responsible for the ground-based ozone measurements with GROMOS-C, performed the data analysis, and
420 prepared the manuscript. ES provided the Aura-MLS data. WK helped with data analysis. GS designed the concept of the study and contributed to the interpretation of the results. All of the authors discussed the scientific findings and provided valuable feedback for manuscript editing.

Acknowledgements. The authors acknowledge NASA Global Modeling and assimilation Office (GMAO) for providing the MERRA-2 reanalysis data and the Aura/MLS team for providing the satellite data. We thank the Swiss Polar Institute (SPI) and the Institute of Applied
425 Physics (IAP) supports the development of the GROMOS-C and MIAWARA-C radiometers.

Financial support. This research has been supported by the Swiss National Science Foundation (grant no. 200021-200517/1).

References

Andrews, D. and Mcintyre, M. E.: Planetary waves in horizontal and vertical shear: The generalized Eliassen-Palm relation and the mean zonal acceleration, Journal of Atmospheric Sciences, 33, 2031–2048, 1976.

430   Baldwin, M. P. and Dunkerton, T. J.: Stratospheric Harbingers of Anomalous Weather Regimes, Science, 294, 581–584, https://doi.org/10.1126/science.1063315, 2001.

Baldwin, M. P., Ayarzagüena, B., Birner, T., Butchart, N., Butler, A. H., Charlton-Perez, A. J., Domeisen, D. I. V., Garfinkel, C. I., Garny, H., Gerber, E. P., Hegglin, M. I., Langematz, U., and Pedatella, N. M.: Sudden Stratospheric Warmings, Reviews of Geophysics, 59, e2020RG000 708, https://doi.org/https://doi.org/10.1029/2020RG000708, e2020RG000708 10.1029/2020RG000708, 2021.

435   Bazhenov, O.: Increased humidity in the stratosphere as a possible factor of ozone destruction in the Arctic during the spring 2011 using Aura MLS observations, International Journal of Remote Sensing, 40, 3448–3460, 2019.

Becker, E.: Dynamical Control of the Middle Atmosphere, Space Science Reviews, 168, 283–314, https://doi.org/10.1007/s11214-011-9841-5, 2012.

Becker, E. and Fritts, D. C.: Enhanced gravity-wave activity and interhemispheric coupling during the MaCWAVE/MIDAS northern summer

440   program 2002, Annales Geophysicae, 24, 1175–1188, https://doi.org/10.5194/angeo-24-1175-2006, 2006.

Bernet, L., Boyd, I., Nedoluha, G., Querel, R., Swart, D., and Hocke, K.: Validation and Trend Analysis of Stratospheric Ozone Data from Ground-Based Observations at Lauder, New Zealand, Remote Sensing, 13, https://doi.org/10.3390/rs13010109, 2021.

Brasseur, G. P. and Solomon, S.: Composition and chemistry, Aeronomy of the Middle Atmosphere: Chemistry and Physics of the Stratosphere and Mesosphere, pp. 265–442, 2005.

445   Brewer, A.: Evidence for a world circulation provided by the measurements of helium and water vapour distribution in the stratosphere, Quarterly Journal of the Royal Meteorological Society, 75, 351–363, 1949.

Brinksma, E. J., Swart, D. P. J., Bergwerff, J. B., Meijer, Y. J., and Ormel, F. T.: RIVM Stratospheric Ozone Lidar at NDSC Station Lauder: Routine Measurements and Validation During the OPAL Campaign, in: Advances in Atmospheric Remote Sensing with Lidar, edited by Ansmann, A., Neuber, R., Rairoux, P., and Wandinger, U., pp. 529–532, Springer Berlin Heidelberg, Berlin, Heidelberg, 1997.

450   Davis, S. M., Hegglin, M. I., Fujiwara, M., Dragani, R., Harada, Y., Kobayashi, C., Long, C., Manney, G. L., Nash, E. R., Potter, G. L., et al.: Assessment of upper tropospheric and stratospheric water vapor and ozone in reanalyses as part of S-RIP, Atmospheric Chemistry and Physics, 17, 12 743–12 778, 2017.

Dobson, G. M. B.: Origin and distribution of the polyatomic molecules in the atmosphere, Proceedings of the Royal Society of London. Series A. Mathematical and Physical Sciences, 236, 187–193, 1956.

455   Eckstein, J., Ruhnke, R., Zahn, A., Neumaier, M., Kirner, O., and Braesicke, P.: An assessment of the climatological representativeness of IAGOS-CARIBIC trace gas measurements using EMAC model simulations, Atmospheric Chemistry and Physics, 17, 2775–2794, 2017.

Eriksson, P., Jiménez, C., and Buehler, S. A.: Qpack, a general tool for instrument simulation and retrieval work, Journal of Quantitative Spectroscopy and Radiative Transfer, 91, 47–64, https://doi.org/https://doi.org/10.1016/j.jqsrt.2004.05.050, 2005.

Eriksson, P., Buehler, S., Davis, C., Emde, C., and Lemke, O.: ARTS, the atmospheric radiative transfer simulator, version 2, Journal of

460   Quantitative Spectroscopy and Radiative Transfer, 112, 1551–1558, https://doi.org/https://doi.org/10.1016/j.jqsrt.2011.03.001, 2011.

Espy, P. J., Ochoa Fernández, S., Forkman, P., Murtagh, D., and Stegman, J.: The role of the QBO in the inter-hemispheric coupling of summer mesospheric temperatures, Atmospheric Chemistry and Physics, 11, 495–502, https://doi.org/10.5194/acp-11-495-2011, 2011.

Fernández, S., Murk, A., and Kämpfer, N.: GROMOS-C, a novel ground-based microwave radiometer for ozone measurement campaigns, Atmospheric Measurement Techniques, 8, 2649–2662, 2015.

465   Flury, T., Hocke, K., Haefele, A., Kämpfer, N., and Lehmann, R.: Ozone depletion, water vapor increase, and PSC generation at midlatitudes by the 2008 major stratospheric warming, Journal of Geophysical Research: Atmospheres, 114, 2009.

Forkman, P., Eriksson, P., Murtagh, D., and Espy, P.: Observing the vertical branch of the mesospheric circulation at latitude 60 N using ground-based measurements of CO and H2O, Journal of Geophysical Research: Atmospheres, 110, 2005.

Gelaro, R., McCarty, W., Suárez, M. J., Todling, R., Molod, A., Takacs, L., Randles, C. A., Darmenov, A., Bosilovich, M. G., Reichle, R.,
470   et al.: The modern-era retrospective analysis for research and applications, version 2 (MERRA-2), Journal of climate, 30, 5419–5454, 2017.

Goldberg, R. A., Fritts, D. C., Williams, B. P., Lübken, F.-J., Rapp, M., Singer, W., Latteck, R., Hoffmann, P., Müllemann, A., Baumgarten, G., Schmidlin, F. J., She, C.-Y., and Krueger, D. A.: The MaCWAVE/MIDAS rocket and ground-based measurements of polar summer dynamics: Overview and mean state structure, Geophysical Research Letters, 31, https://doi.org/https://doi.org/10.1029/2004GL019411,
475   2004.

Graf, M., Scheidegger, P., Kupferschmid, A., Looser, H., Peter, T., Dirksen, R., Emmenegger, L., and Tuzson, B.: Compact and lightweight mid-infrared laser spectrometer for balloon-borne water vapor measurements in the UTLS, Atmospheric Measurement Techniques, 14, 1365–1378, https://doi.org/10.5194/amt-14-1365-2021, 2021.

Inness, A., Chabrillat, S., Flemming, J., Huijnen, V., Langenrock, B., Nicolas, J., Polichtchouk, I., and Razinger, M.: Exceptionally low Arctic
480   stratospheric ozone in spring 2020 as seen in the CAMS reanalysis, Journal of Geophysical Research: Atmospheres, 125, e2020JD033 563, 2020.

Karlsson, B., Körnich, H., and Gumbel, J.: Evidence for interhemispheric stratosphere-mesosphere coupling derived from noctilucent cloud properties, Geophysical Research Letters, 34, https://doi.org/https://doi.org/10.1029/2007GL030282, 2007.

Knowland, K. E., Keller, C. A., Wales, P. A., Wargan, K., Coy, L., Johnson, M. S., Liu, J., Lucchesi, R. A., Eastham, S. D., Fleming, E., et al.:
485   NASA GEOS Composition Forecast Modeling System GEOS-CF v1. 0: Stratospheric Composition, Journal of advances in modeling earth systems, 14, 2022.

Körnich, H. and Becker, E.: A simple model for the interhemispheric coupling of the middle atmosphere circulation, Advances in Space Research, 45, 661–668, 2010.

Lambert, A., Read, W., , and Livesey, N.: MLS/Aura Level 2 Water Vapor (H2O) Mixing Ratio V004, Greenbelt, MD, USA, Goddard Earth
490   Sciences Data and Information Services Center (GES DISC), https://doi.org/10.5067/Aura/MLS/DATA2009, 2015.

Langematz, U.: Stratospheric ozone: down and up through the anthropocene, ChemTexts, 5, 1–12, 2019.

Lawrence, Z. D., Perlwitz, J., Butler, A. H., Manney, G. L., Newman, P. A., Lee, S. H., and Nash, E. R.: The remarkably strong Arctic stratospheric polar vortex of winter 2020: Links to record-breaking Arctic oscillation and ozone loss, Journal of Geophysical Research: Atmospheres, 125, e2020JD033 271, 2020a.

495   Lawrence, Z. D., Perlwitz, J., Butler, A. H., Manney, G. L., Newman, P. A., Lee, S. H., and Nash, E. R.: The remarkably strong Arctic stratospheric polar vortex of winter 2020: Links to record-breaking Arctic oscillation and ozone loss, Journal of Geophysical Research: Atmospheres, 125, e2020JD033 271, 2020b.

Lee, J. N., Wu, D. L., Manney, G. L., Schwartz, M. J., Lambert, A., Livesey, N. J., Minschwaner, K. R., Pumphrey, H. C., and Read, W. G.: Aura Microwave Limb Sounder observations of the polar middle atmosphere: Dynamics and transport of CO and H2O, Journal of
500   Geophysical Research: Atmospheres, 116, 2011.

Lindzen, R. S.: Turbulence and stress owing to gravity wave and tidal breakdown, Journal of Geophysical Research: Oceans, 86, 9707–9714, https://doi.org/10.1029/JC086iC10p09707, 1981.

Livesey, N., Van Snyder, W., Read, W., and Wagner, P.: Retrieval algorithms for the EOS Microwave limb sounder (MLS), IEEE Transactions on Geoscience and Remote Sensing, 44, 1144–1155, https://doi.org/10.1109/TGRS.2006.872327, 2006.

505 Lossow, S., Khaplanov, M., Gumbel, J., Stegman, J., Witt, G., Dalin, P., Kirkwood, S., Schmidlin, F., Fricke, K., and Blum, U.: Middle atmospheric water vapor and dynamics in the vicinity of the polar vortex during the Hygrosonde-2 campaign, Atmospheric Chemistry and Physics, 9, 4407–4417, 2009.

Matsuno, T.: A Dynamical Model of the Stratospheric Sudden Warming, Journal of the Atmospheric Sciences, 28, 1479–1494, https://doi.org/10.1175/1520-0469(1971)028<1479:ADMOTS>2.0.CO;2, 1971.

510 Matthias, V., Dörnbrack, A., and Stober, G.: The extraordinarily strong and cold polar vortex in the early northern winter 2015/2016, Geophysical Research Letters, 43, 12,287–12,294, https://doi.org/https://doi.org/10.1002/2016GL071676, 2016.

Matthias, V., Stober, G., Kozlovsky, A., Lester, M., Belova, E., and Kero, J.: Vertical structure of the Arctic spring transition in the middle atmosphere, Journal of Geophysical Research: Atmospheres, 126, e2020JD034 353, 2021.

McConnell, J. C. and Jin, J. J.: Stratospheric ozone chemistry, Atmosphere-Ocean, 46, 69–92, 2008.

515 Orsolini, Y. J., Urban, J., Murtagh, D. P., Lossow, S., and Limpasuvan, V.: Descent from the polar mesosphere and anomalously high stratopause observed in 8 years of water vapor and temperature satellite observations by the Odin Sub-Millimeter Radiometer, Journal of Geophysical Research: Atmospheres, 115, 2010.

Rodgers, C. D.: Inverse methods for atmospheric sounding: theory and practice, vol. 2, World scientific, 2000.

Ryan, N. J., Kinnison, D. E., Garcia, R. R., Hoffmann, C. G., Palm, M., Raffalski, U., and Notholt, J.: Assessing the ability to derive 520 rates of polar middle-atmospheric descent using trace gas measurements from remote sensors, Atmospheric Chemistry and Physics, 18, 1457–1474, https://doi.org/10.5194/acp-18-1457-2018, 2018.

Scheiben, D., Schanz, A., Tschanz, B., and Kämpfer, N.: Diurnal variations in middle-atmospheric water vapor by ground-based microwave radiometry, Atmospheric chemistry and physics, 13, 6877–6886, 2013.

Scheiben, D., Tschanz, B., Hocke, K., Kämpfer, N., Ka, S., and Oh, J.: The quasi 16-day wave in mesospheric water vapor during boreal 525 winter 2011/2012, Atmospheric chemistry and physics, 14, 6511–6522, 2014.

Schranz, F., Tschanz, B., Rüfenacht, R., Hocke, K., Palm, M., and Kämpfer, N.: Investigation of Arctic middle-atmospheric dynamics using 3 years of H_2O and O_3 measurements from microwave radiometers at Ny-Ålesund, Atmospheric Chemistry and Physics, 19, 9927–9947, https://doi.org/10.5194/acp-19-9927-2019, 2019.

Schranz, F., Hagen, J., Stober, G., Hocke, K., Murk, A., and Kämpfer, N.: Small-scale variability of stratospheric ozone during the sudden 530 stratospheric warming 2018/2019 observed at Ny-Ålesund, Svalbard, Atmospheric chemistry and physics, 20, 10 791–10 806, 2020.

Schwartz, M., Froidevaux, L., Livesey, N., and Read, W.: MLS/Aura Level 2 Ozone (O3) Mixing Ratio V004, Greenbelt, MD, USA, Goddard Earth Sciences Data and Information Services Center (GES DISC), https://doi.org/10.5067/Aura/MLS/DATA2017, 2015a.

Schwartz, M., Froidevaux, L., Livesey, N., and Read, W.: MLS/Aura Level 2 Temperature V004, Greenbelt, MD, USA, Goddard Earth Sciences Data and Information Services Center (GES DISC), https://doi.org/10.5067/Aura/MLS/DATA2021, 2015b.

535 Sica, R. J. and Haefele, A.: Retrieval of temperature from a multiple-channel Rayleigh-scatter lidar using an optimal estimation method, Appl. Opt., 54, 1872–1889, https://doi.org/10.1364/AO.54.001872, 2015.

Sica, R. J. and Haefele, A.: Retrieval of water vapor mixing ratio from a multiple channel Raman-scatter lidar using an optimal estimation method, Appl. Opt., 55, 763–777, https://doi.org/10.1364/AO.55.000763, 2016.

Smith, A., Pedatella, N., and Mullen, Z.: Interhemispheric coupling mechanisms in the middle atmosphere of WACCM6, Journal of the Atmospheric Sciences, 77, 1101–1118, 2020a.

Smith, A. K.: Global Dynamics of the MLT, Surveys in Geophysics, 33, 1177–1230, https://doi.org/10.1007/s10712-012-9196-9, 2012.

Smith, A. K., Pedatella, N. M., and Mullen, Z. K.: Interhemispheric Coupling Mechanisms in the Middle Atmosphere of WACCM6, Journal of the Atmospheric Sciences, 77, 1101 – 1118, https://doi.org/10.1175/JAS-D-19-0253.1, 2020b.

Solomon, S., Haskins, J., Ivy, D. J., and Min, F.: Fundamental differences between Arctic and Antarctic ozone depletion, Proceedings of the National Academy of Sciences, 111, 6220–6225, 2014.

Stober, G., Matthias, V., Jacobi, C., Wilhelm, S., Höffner, J., and Chau, J. L.: Exceptionally strong summer-like zonal wind reversal in the upper mesosphere during winter 2015/16, Annales Geophysicae, 35, 711–720, https://doi.org/10.5194/angeo-35-711-2017, 2017.

Straub, C., Murk, A., and Kämpfer, N.: MIAWARA-C, a new ground based water vapor radiometer for measurement campaigns, Atmospheric Measurement Techniques, 3, 1271–1285, https://doi.org/10.5194/amt-3-1271-2010, 2010.

Straub, C., Tschanz, B., Hocke, K., Kämpfer, N., and Smith, A. K.: Transport of mesospheric H 2 O during and after the stratospheric sudden warming of January 2010: observation and simulation, Atmospheric chemistry and physics, 12, 5413–5427, 2012.

Tritscher, I., Pitts, M. C., Poole, L. R., Alexander, S. P., Cairo, F., Chipperfield, M. P., Grooß, J.-U., Höpfner, M., Lambert, A., Luo, B., et al.: Polar stratospheric clouds: Satellite observations, processes, and role in ozone depletion, Reviews of geophysics, 59, e2020RG000 702, 2021.

Tschanz, B., Straub, C., Scheiben, D., Walker, K. A., Stiller, G. P., and Kämpfer, N.: Validation of middle-atmospheric campaign-based water vapour measured by the ground-based microwave radiometer MIAWARA-C, Atmospheric Measurement Techniques, 6, 1725–1745, https://doi.org/10.5194/amt-6-1725-2013, 2013.

Waibel, A., Peter, T., Carslaw, K., Oelhaf, H., Wetzel, G., Crutzen, P., Poschl, U., Tsias, A., Reimer, E., and Fischer, H.: Arctic ozone loss due to denitrification, Science, 283, 2064–2069, 1999.

Wargan, K., Labow, G., Frith, S., Pawson, S., Livesey, N., and Partyka, G.: Evaluation of the ozone fields in NASA's MERRA-2 reanalysis, Journal of Climate, 30, 2961–2988, https://doi.org/10.1175/JCLI-D-16-0699.1, 2017.

Waters, J. W., Froidevaux, L., Harwood, R. S., Jarnot, R. F., Pickett, H. M., Read, W. G., Siegel, P. H., Cofield, R. E., Filipiak, M. J., Flower, D. A., Holden, J. R., Lau, G. K., Livesey, N. J., Manney, G. L., Pumphrey, H. C., Santee, M. L., Wu, D. L., Cuddy, D. T., Lay, R. R., Loo, M. S., Perun, V. S., Schwartz, M. J., Stek, P. C., Thurstans, R. P., Boyles, M. A., Chandra, K. M., Chavez, M. C., Chen, G.-S., Chudasama, B. V., Dodge, R., Fuller, R. A., Girard, M. A., Jiang, J., Jiang, Y., Knosp, B. W., LaBelle, R. C., Lam, J. C., Lee, K., Miller, D., Oswald, J. E., Patel, N. C., Pukala, D. M., Quintero, O., Scaff, D. M., Snyder, W. V., Tope, M. C., Wagner, P. A., and Walch, M. J.: The Earth observing system microwave limb sounder (EOS MLS) on the aura Satellite, IEEE Transactions on Geoscience and Remote Sensing, 44, 1075–1092, 2006.

Zahn, A., Christner, E., van Velthoven, P., Rauthe-Schöch, A., and Brenninkmeijer, C.: Processes controlling water vapor in the upper troposphere/lowermost stratosphere: An analysis of 8 years of monthly measurements by the IAGOS-CARIBIC observatory, Journal of Geophysical Research: Atmospheres, 119, 11–505, 2014.

Zuber, R., Köhler, U., Egli, L., Ribnitzky, M., Steinbrecht, W., and Gröbner, J.: Total ozone column intercomparison of Brewers, Dobsons, and BTS-Solar at Hohenpeißenberg and Davos in 2019/2020, Atmospheric Measurement Techniques, 14, 4915–4928, https://doi.org/10.5194/amt-14-4915-2021, 2021.